POLITECNICO
MILANO 1863

SCUOLA DI INGEGNERIA INDUSTRIALE
E DELL'INFORMAZIONE

Study of Surface Electrocatalytic Processes by Ultrafast X-ray Diffraction

Tesi di Laurea Magistrale in
Physics Engineering - Ingegneria Fisica

Author: **Meryem Ennaji**

Student ID: 947234
Advisor: Prof. Marco Moretti
Co-advisors: Dr. Jakub Drnec
Academic Year: 2022-2023

Abstract

In the field of sustainable energy technology today, nanostructured materials are pivotal in facilitating electrochemical reactions, with particular emphasis placed on Platinum nanoparticles (Pt NP). Platinum, in fact, assumes a critical role in electrochemistry as it stands as the most active element for numerous essential electrocatalytic reactions. Furthermore, in the context of electrochemical energy conversion and storage, such as in polymer electrolyte membrane fuel cells (PEMFCs), it maintains its status as the most important catalyst for applications and continues to serve as the standard for electrocatalyst materials.

The oxidation of the Pt surface directly impacts the separate processes of Pt dissolution and oxygen reduction, lowering the longevity and efficiency of the Pt catalysts. An understanding of the dynamic surface chemistry on electrochemically active Pt NP from a time-resolved perspective is therefore valuable. In this study, Pt NP inside commercial hydrogen fuel cell catalyst layers are studied in situ, using time-resolved high-energy powder X-ray diffraction. Advances in electrochemical cell design significantly increase the quality of diffraction patterns obtained. A fuel cell designed in order to guarantee fast diffusion of reactants to the electrode surface and very close electrodes has been used. This polymer electrolyte membrane fuel cell (PEMFC) design combined with compensation techniques for the ohmic drop correction made the detection of phenomena that are way faster of the PEMFC time constant possible.

The rates and mechanisms of electrochemical reactions occurring at electrodes are studied thanks to two techniques: Potential Step (PS) and Cyclic Voltammetry (CV). The high brilliance 4th generation synchrotron source at the European Synchrotron Radiation Facility (ESRF) it is used for the fundamental understanding of the materials behavior under electrochemical conditions. Rietveld refinement of the lattice parameter and peak intensities of the Pt NP has been performed on TOPAS, a powerful suite of software that allows the sequential analysis of powder diffraction data.

The refined parameters, in particular the lattice parameter, obtained from the study of diffraction patterns collected under several PS has been monitored and studied. For the first time, the time constants characterizing the Double Layer reorganization have been calculated, the charging time constant is 0.0084 ± 0.005 s and the discharging time constant corresponds to 0.0064 ± 0.0042 s. Different time constants at different potentials are also calculated, monitoring the time scale of different electrochemical processes happening on Pt NP surface: adsorption of oxygenated species, place exchange (PE) and adsorption of underpotentially deposited hydrogen. Evidence was given of the different kinetics involving those different phenomena, PE was confirmed to have a very slow kinetics, charging and discharging time constants are: 0.0437 ± 0.0034 s and 0.0226 ± 0.0035. The scale parameter for this PS was sensitive just to PS involving PE.

In the case of CV, the considered refined parameter has been the scale, which is a parameter proportional to the total number of illuminated Pt atoms in the metallic crystal lattice. The diffraction patterns have been collected during CV at different scan rates. Cyclic Voltammograms and scale plots corresponding to the different scan rates have been studied. Evidence was given on support of a very new idea regarding electrochemical surface oxidation. Calculating the charge accumulated and the values of the scale factor at potential 1.1V, for each of the CV studied, was seen that the charge transfer related to the formation of adsorbed oxygen-containing species strongly depends on the scan rates whereas fast extraction process depends very little on sweep rate, which shows that the extraction is driven by potential, independently of the adsorbed species around it.

Keywords: electrochemistry, platinum, fuel cell, potential step, cyclic voltammetry, TOPAS, synchrotron radiation, high energy X-rays.

Abstract in lingua italiana

Nel campo della tecnologia dell'energia sostenibile oggi, i materiali nanostrutturati sono cruciali per facilitare le reazioni elettrochimiche, con particolare enfasi posta sulle nanoparticelle di platino (Pt NP). Il platino, infatti, assume un ruolo critico nell'elettrochimica in quanto è l'elemento più attivo per numerose importanti reazioni elettrocatalitiche. Inoltre, nel contesto della conversione e dello stoccaggio dell'energia elettrochimica, come nelle celle a combustibile a membrana elettrolitica polimerica (PEMFC), mantiene il suo status di catalizzatore più importante per le applicazioni e continua a servire come standard per i materiali elettrocatalitici.

L'ossidazione della superficie del platino influenza direttamente i distinti processi di dissoluzione del platino e riduzione dell'ossigeno, abbassando la longevità e l'efficienza dei catalizzatori al platino. Una comprensione della dinamica chimica superficiale delle Pt NP elettrochimicamente attive da una prospettiva temporale è quindi preziosa. In questo studio, le Pt NP all'interno dei strati di catalizzatore delle celle a combustibile all'idrogeno sono state studiate in situ, utilizzando la diffrazione di raggi X ad alta energia a risoluzione temporale. Gli avanzamenti nella progettazione delle celle elettrochimiche aumentano significativamente la qualità dei modelli di diffrazione ottenuti. È stata utilizzata una cella a combustibile progettata per garantire una rapida diffusione dei reagenti sulla superficie dell'elettrodo e con elettrodi molto vicini. Questa progettazione di celle a combustibile a membrana elettrolitica polimerica (PEMFC) combinata con tecniche di correzione della caduta ohmica ha reso possibile la rilevazione di fenomeni che sono molto più veloci della costante di tempo delle PEMFC.

Le velocità e i meccanismi delle reazioni elettrochimiche che si verificano sugli elettrodi vengono studiati grazie a due tecniche: il Passo di Potenziale (PS) e la Voltammetria Ciclica (CV). La sorgente di sincrotrone di quarta generazione ad alta brillanza presso l'European Synchrotron Radiation Facility (ESRF) è utilizzata per la comprensione fondamentale del comportamento dei materiali in condizioni elettrochimiche. L'analisi di Rietveld dei parametri del reticolo e delle intensità dei picchi delle Pt NP è stata eseguita

su TOPAS, un potente insieme di software che consente l'analisi sequenziale dei dati di diffrazione.

I parametri raffinati, in particolare il parametro del reticolo, ottenuti dallo studio dei modelli di diffrazione raccolti in diversi PS, sono stati monitorati e studiati. Per la prima volta, sono stati calcolate le costanti di tempo che caratterizzano la riorganizzazione del Doppio Strato, la costante di tempo di carica è di 0,0084 ± 0,005 s e la costante di tempo di scarica corrisponde a 0,0064 ± 0,0042 s. Sono state calcolate anche le diverse costanti di tempo a diversi potenziali, monitorando la scala temporale di diversi processi elettrochimici che si verificano sulla superficie delle Pt NP: adsorbimento di specie ossigenate, scambio di posizione (PE) e adsorbimento di idrogeno depositato sotto il potenziale. È stata fornita evidenza delle diverse cinematiche che coinvolgono questi diversi fenomeni, il PE è stato confermato avere una cinematica molto lenta, le costanti di tempo di carica e scarica sono: 0,0437 ± 0,0034 s e 0,0226 ± 0,0035. Il parametro di scala per questo PS era sensibile solo ai PS che coinvolgevano il PE.

Nel caso della CV, il parametro raffinato considerato è stato la scala, che è un parametro proporzionale al numero totale di atomi di platino illuminati nel reticolo cristallino metallico. I modelli di diffrazione sono stati raccolti durante la CV a diverse velocità di scansione. Sono stati studiati Voltammogrammi Ciclici e grafici di scala corrispondenti alle diverse velocità di scansione. È stata fornita evidenza a sostegno di una nuova idea riguardo all'ossidazione superficiale elettrochimica. Calcolando la carica accumulata e i valori del fattore di scala a un potenziale di 1,1 V, per ciascuna delle CV studiate, è emerso che il trasferimento di carica legato alla formazione di specie contenenti ossigeno adsorbite dipende fortemente dalle velocità di scansione, mentre il processo di estrazione rapida dipende molto poco dalla velocità di sweep, il che mostra che l'estrazione è guidata dal potenziale, indipendentemente dalle specie adsorbite intorno ad esso.

Parole chiave: elettrochimica, platino , fuel cell, step di potenziale, ciclovoltammetria, TOPAS, radiazione di sincrotrone, raggi x ad alta energia.

Contents

1 | Introduction

1.1. Aim of the project

With the term energy transition we mean a gradual and steady shift of global energy use from fossil-based sources to a zero-carbon system by 2050, according to the International Renewable Energy Agency (IRENA) [5]. The energy transition is one of the great challenges of the society of our time. In order to limit the climate change global, greenhouse-gas emissions must be drastically reduced.

A transition to sustainable energy is needed, it is in the field of sustainable energy technologies that electrochemical reactions on nanostructured materials play a key role. Indeed, the explosion in both academic and industrial interest in these materials over the past decade arises from the fact that because of their dimensions at the nanoscale, they often exhibit enhanced electrochemical performance compared to their bulk counterparts. They result to be ideal for example for: electrocatalysis, energy storage, electrosynthesis, etc.

Nanostructured materials such as platinum nanoparticles (Pt NPs) serve as catalysts in both the anode and cathode, enhancing those electrochemical reactions involved in generating electricity from hydrogen and oxygen in Polymer electrolyte membrane fuel cell (PEMFC). In the case of heterogeneous catalysis, where the reactions occur onto the catalyst surface, the most promising approach in material design follows the Sabatier principle: the ability of the surface to bind adsorbates and the strength of the bonds define the reaction thermodynamics and kinetics [24]. In this respect, the catalyst surface chemistry and structure (crystallographic orientation of the facets and/or strain) are used as levers to optimize its performance.

The present project has the objective of studying the kinetics of fast fundamental processes taking place at the surface of nanostructured electrocatalyst electrodes. We will take advantage of the high brilliance 4th generation synchrotron source at ESRF for the fundamental understanding of the materials behavior under electrochemical conditions. We will focus mainly on two processes: electric double layer restructuring and adsorption/desorption of small molecules. As a model system we will use a standard catalyst

material used in low temperature hydrogen fuel cells, consisting of very small Pt NP's supported on carbon particles.

1.2. Electrochemistry: introduction

Electrochemistry is the study of structures and processes at the interface between an electronic conductor (*the electrode*) and an ionic conductor (*the electrolyte*) or at the interface between two electrolytes [41].
Metals and semiconductors are common examples of electronic conductors, and under certain circumstances even insulators can be made electronically conducting, for example by photoexcitation, these materials will be used as electrodes. Electrolyte solutions, molten salts including ionic liquids, and solid electrolytes are ionic conductors.
Let's now consider what happens in an electrochemical system in which there are two regions separated by an interface [22]. The flow rate or movement of charged species across that interface is given by the quantity of charged particles passing through a unit area per unit time. The flux, $\boldsymbol{J}$, of species j is commonly expressed in units of moles per square meter per second ($mol{\cdot}cm^{-2}{\cdot}\ s^{-1}$) and is:

$$J_j = -\left(\frac{C_j D_j}{RT}\right)\nabla\bar{\mu}_j \tag{1.1}$$

Where the terms C_j ($mol{\cdot}cm^{-3}$) and D_j ($cm^2{\cdot}s^{-1}$) are the concentration and diffusion of the species j. And R is the gas constant ($J{\cdot}K^{-1}mol^{-1}$) and T is the temperature (K). The term $\nabla\bar{\mu}_j$ represent the spatial gradient of the electrochemical potential. It can be seen as the generalized force that "displaces mass" or better saying charged species.
A very important concept has just been introduced: flux is driven by the electrochemical potential difference between two regions. Charged species tend to move from areas of higher electrochemical potential to lower electrochemical potential. Electrochemical equilibrium is reached when for all species j, the equation $\nabla\bar{\mu}_j = 0$ is valid.
We can notice that the magnitude of the flux is influenced by factors such as concentration, diffusion, and the presence of an electric field or potential gradient. The first two terms are included in the coefficients introduced before whereas for the other terms we have to introduce a new definition.
The electrochemical potential for species j can be conceptually subdivided in two distinct terms accounting the effects of chemical potential (related to concentration or activity) and electrical potential (related to the electric field).

$$\bar{\mu_j^\alpha} = \mu_j^\alpha + z_j F\phi^\alpha \tag{1.2}$$

The term μ_j^α is the chemical potential of j, relative to a reference state, and $z_j F\phi^\alpha$ is the electrostatic energy per mole of j in phase α, relative to a reference state.
The chemical potential term is rate of change of any thermodynamic potentials with N, number of particles, when all the other relevant variables are fixed:

$$\bar{\mu}_j^\alpha = \left(\frac{\partial E}{\partial N}\right)_{S,V} = \left(\frac{\partial H}{\partial N}\right)_{S,P} = \left(\frac{\partial F}{\partial N}\right)_{T,V} = \left(\frac{\partial G}{\partial N}\right)_{T,P} \tag{1.3}$$

Where from the last equation we can derive that the chemical potential can be seen as the Gibbs free energy per particle, meaning that the chemical potential is the work required to add a particle to the system at constant pressure and temperature [37].

1.2.1. Electric Double-Layer

So far, we have given a first introduction to electrochemistry, now we will focus on electrocatalytic reactions, namely those reactions, oxidation and reduction, involving interactions of reactants with the electrode surface [33]. In order to understand these reactions we first have to consider that what we are considering are open systems, namely systems in which particles move in and out until the chemical potential of the system equals that of the surroundings [37]. For this type of systems we need a statistical approach that follows the grand canonical distribution function. Moreover in order to comprehend the principles of electrocatalytic reactions we need to consider that they occur at the interface between an electrode and an electrolyte where an electric double layer (EDL) forms [31].
Let's now concentrate in understanding this last introduced concept.
Let's consider the most important electrochemical system: a metal electrode in equilibrium with a redox couple with both the oxidized (O) and reduced (R) form present dissolved in an inert electrolyte, for the sake of simplicity we consider that no electrochemical reactions take place.
In figure 1.1 we can see the different steps that lead to to the reaching of electrochemical equilibrium through the system.

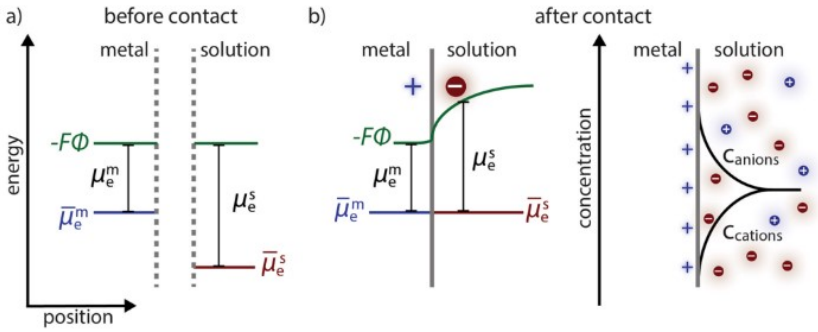

Figure 1.1: Electrochemical equilibrium at an electrode-electrolyte interface. [22]

Before the contact (a), an electron experiences different electrochemical potential values depending if it's in the metal electrode or in the solution. This difference translates in a gradient in the electrochemical potential at the interface between the metal and the electrolyte once they are brought into contact (b).
As we have seen before the presence of a a gradient in the electrochemical potential across the interface causes the charge transfer. For this reason the metal surface carries an excess charge, because of electroneutrality principle a charge of equal magnitude and opposite sign rises up on the solution side of the interface.
By looking at the right image in part (b) of figure 1.1 we can see that there is a deficit of electrons on the metal surface that is balanced by a greater quantity of anions than cations on the solution side of the interface. In this equilibration process we have to consider that the metal electrode is an excellent conductor, its excess charge is restricted to a surface region of about 1 $\mathring{A}$ thick. On the electrolyte side we have a lower carrier concentration with respect to the metal and so the charge in the solution extends over a larger region of space, typically 5–20 $\mathring{A}$ thick.
The resulting charge distribution of two narrow regions of equal and opposite charge is known as the electric double layer.
The electric double layer (EDL) is is one of the focal point of electrochemistry, it is the most important region for electrochemical and heterogeneous catalysis.
Here, we will briefly review classical theoretical attempts to describe aspects of the EDL [42][31][26].
The first EDL model was proposed by Helmholtz in 1853, he was the first realizing that a charged electrode attracts counter-ions from the electrolyte. The surface charge on the electrode will cause a surface potential (ϕ) that drops linearly in the electrolyte, in the first ionic layer and at the end of this layer the same potential as in the bulk electrolyte is observed. This make this structure so similar to parallel plane capacitor. The separation between the two parallel planes is given by the counter-ion radius, yielding a capacitance

that is larger than the typical value of a dielectric capacitor by many orders of magnitude. This is the reason why EDL capacitors hold great promise for the next generation of electrical energy storage, deionization, blue-energy harvesting, and many other technological applications.

It is a very simple model that describes charge separation and predicts the capacitance of EDL in a proper way but doesn't give information about the microscopic details of the electrode-electrolyte interface, indeed does not consider the thermic motion of the ions in the solution.

The idea is that when charged fluids are taken into consideration we cannot apply Van der Waals model since for this simple mean field approach the fluid is assumed to be completely uniform, that means no spatial correlations between the particles. So we need to introduce ion–ion interaction in our model, this is done by following the Debye-Hückel theory [37]. This theory indeed finds a solution to the strongly unlinear Poisson–Boltzmann(PB) equation:

$$\nabla^2\psi(r) = -\frac{1}{\epsilon V}\sum_j q_j N_j exp[-\beta q_j \psi(r)] \tag{1.4}$$

Where we are considering a system made of several species of charged particles in a volume V , and N_j is the total number of particles of type j and q_j, the electric charge carried by each one of these particles. With ψ we identify the value of the electrostatic potential generated by all the charges and with β the Boltzmann factor. In order to linearize the PB equation we consider that the kinetic energy of the ions is much larger than their electrostatic potential energy, meaning $q_j\psi \ll k_B T$.

We obtain the Debye-Hückel(DH) equation:

$$\nabla^2\psi(r) = -\frac{1}{\lambda_{DH}^2}\psi(r) = 0 \tag{1.5}$$

where

$$\lambda_{DH} = \sqrt{\frac{\epsilon V k_B T}{\sum_j N_j q_j^2}} \tag{1.6}$$

Solving the DH equation in spherical coordinates we obtain the general solution for the potential:

$$\psi(r) = \frac{q}{4\pi\epsilon r} exp(-\kappa r) \tag{1.7}$$

where $\kappa = 1/\lambda_{DH}$ is called the screening parameter. The Debye-Hückel length is defined as the thickness of the ionic cloud around the center ion. The total charge of this cloud has the same modulus as the central ion charge, but the signal is the opposite, which guarantees electroneutrality.

Inspired by Debye-Hückel model Gouy and Chapman proposed the diffuse layer model (1909-1913). Which for small charge densities at the electrode leads to an exponentially decreasing electric potential.
However the Gouy and Chapman theory has some limitations indeed, it considers that ions are punctual charges which is not true since in the solution they have the solvation shell. Moreover, for high electrolyte concentrations, it shows some deviations from experimental observations.
It was Stern that in 1924 suggested to use a combination of the Helmholtz and Gouy-Chapman models for an improved description of the EDL. He basically proposed a combination of linearly and exponentially decreasing potentials within the double layer region, so that the electrolyte region is now virtually devided into an inner layer not accessible to the ionic species (the Stern layer) and a diffuse layer accounting for the inhomogeneous ion distributions.

The EDL is comprised of a compact layer of specifically absorbed water molecules and ions, and a diffuse layer that characterizes a region of continuously decreasing counterion concentration from the dense compact layer to the nominal bulk solution.

The Stern model still has limitations. So that Grahame in 1947 extended the Stern model by proposing a distinction between inner and outer Helmholtz planes (IHP and OHP) according to their closest distances from the electrode surface. The first layer is a compact layer of specifically absorbed water molecules and ions, strongly attracted to the electrode's surface. Beyond the inner Helmholtz layer, there is a region where ions are distributed more loosely and not strongly bound to the electrode. This region is called the diffuse layer or the outer Helmholtz plane. In figure 1.2 we find a very nice sum up of the theories introduced.

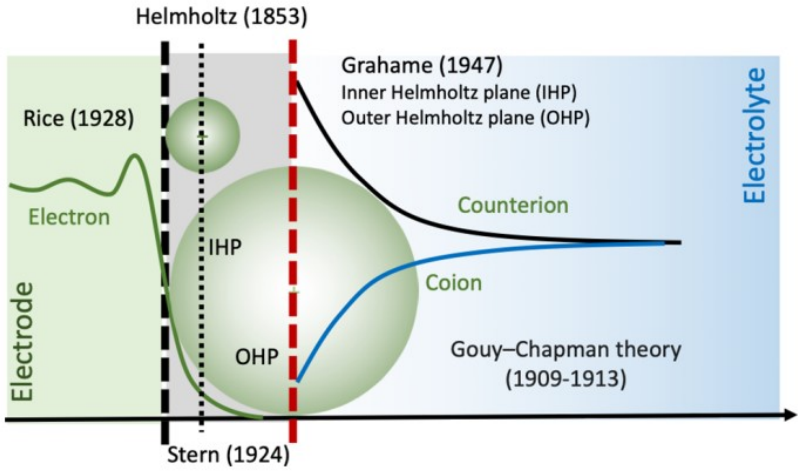

Figure 1.2: Classical models of the electric double layer (EDL) [42].

1.2.2. Metal Oxidation and Oxide Film Formation

The formation of an oxide film on the electrode surface is a natural process that is driven by the electrochemical reactions occurring at the electrode-electrolyte interface.
The study of oxide-film formation at noble transition metals provides an important transition case between pure, 2-dimensional surface processes of OH or 0 chemisorption, and formation and growth of 3-dimensional bulk oxide films or phases [25]. So when the metal is used at the electrode in an electrochemical cell (a complete explanation of this this type of device is in section 1.3) and exposed to an electrolyte, oxidation reactions take place:

$$M \rightarrow M^z + ze^- \tag{1.8}$$

where M identifies the metal, z the metal's oxidation state and ze^- represents z moles of electrons. The products of this reaction is given by metal cations and electrons. By coupling this reaction with hydrolysis of the cations leads to the formation of a poorly adherent oxide film:

$$M^z + zH_20 \rightarrow MO_z^{2-} + 2H_2 \tag{1.9}$$

The mechanism described above, where metal cations dissolve from the metal surface (dissolution) and then react with the environment to form metal oxide compounds (precipitation), is indeed often referred to as *dissolution and precipitation*. Dissolution refers to the process of metal atoms or ions leaving the metal surface and entering the surrounding electrolyte. This extraction process is a crucial step in the corrosion process. The dissolved metal cations then react with oxygen, water, or other chemical species in the environment, leading to the formation of metal oxide compounds on the metal surface.

Another process that can take place at the electrode surface is the direct oxide film formation by nucleation and growth. At certain sites on the metal surface, oxide species start to form and cluster together. These initial clusters are known as nuclei. Once the nuclei are formed, oxide species from the surrounding environment or electrolyte deposit onto these nuclei, causing the oxide film to grow layer by layer.
When a mono layer of OH or O is formed on the metal surface in the form of a 2-dimensional array, field-dependent interchange between metal atoms in the surface and OH or 0 species in the ad-layer contribute to continuing oxidation and growth of the film. It is the so-called *place-exchange* phenomenon, a metal surface atom exchanges with an oxygen species [27]. In figure 1.3 a clear schematic of the phenomenon is given. In the place exchange process (PE) a metal atom, let's consider Platinum,Pt_{sur}, is lifted out of the topmost layer without in-plane displacement going to the PE layer, Pt_{PE}. An oxygen atom (dark red) that was previously adsorbed on top of surface moves into the formed vacancy site [32].

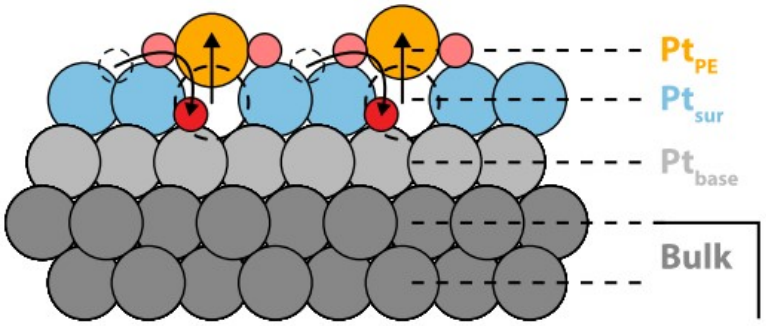

Figure 1.3: Schematic of the Place Exchange process. [32]

1.3. The Fuel Cell

A fuel cell is an electrochemical energy converter, namely it converts the energy of a chemical reaction into electrical energy [9].
There are several reasons why we are interested in studying this technology that is gaining so much interest scientific and industrial communities. Fuel cells are very promising systems due to the versatility of their usu, indeed,they could provide significant benefits for our environment, health and development[10].
So let's try to understand why this technology is gaining so much interest. Fuel cells are very energy efficient devices for extracting power from fuels. Also this power supply is characterized by good reliability meaning that the quality of power produced doesn't degrade over time. Considering that there are no moving parts fuel cells are much more silent than conventional energy production. Moreover, if we consider hydrogen fuel cells, they can produce electricity till a constant supply of fuel (hydrogen) and an oxidising agent (oxygen) is provided. As a result, until the supply of fuel and oxygen is shut off, these cells can continue to generate power. And above all, fuel cells produce electricity through electrochemical reactions, and depending on the fuel source, they can significantly reduce greenhouse gas emissions compared to fossil fuel-based power plants and vehicles. For all these advantages there are still some disadvantages and technological limits to be mentioned. The cost of the catalysts is very high since precious metals are used such as platinum this makes the manufacture very expensive. Another key point is connected to the need of implementation of infrastructures for the storage and transportation of hydrogen.
Moreover, hydrogen is the most abundant element in the universe, but doesn't exist on its own and so it must be separated from the other elements in the molecules where it occurs. The two most common methods for producing hydrogen are steam-methane reforming and separation from carbon fossil fuels, or extraction from water via electrolysis. The first method is the most common method for large-scale hydrogen production. It involves reacting methane with steam in the presence of a catalyst, the reaction produces hydrogen along with carbon monoxide and carbon dioxide. Therefore, the carbon footprint of hydrogen produced is high due to the CO_2 emissions. Only thinking of coupling this method with carbon capture and storage technology, can reduce its environmental impact. Another problem to face is the risk of methane leakage during the extraction, transportation, and processing.
For what concerns electrolysis, electricity is used to split water into hydrogen(H_2) and oxygen (O_2) through an electrochemical reaction. It is a very interesting method for hydrogen production, particularly when coupled with renewable energy sources, but it also

has some limitations. In order to split water a significant amount of electricity is required, if the electricity used is generated from fossil fuels it is easy to understand that we are almost back to zero. Also, the cost of electricity is a significant factor in determining the overall high cost of hydrogen produced through electrolysis.
Another significant challenge is the longevity of materials in fuel cells. Indeed those exposed to high temperatures and chemical reactions may suffer from degradation and corrosion. Over time, catalysts can degrade due to chemical processes, contamination, or poisoning, leading to a decline in fuel cell performance.
Scientific research aims to understand and to make all these limitations less impactful in order to make the commercialization on large scale possible and utilise them in a huge variety of applications.

There are several types of fuel cells, differentiated primarily by the kind of electrolyte they employ. This classification determines the kind of electrochemical reactions that take place in the cell, the required catalysts, the operating temperature, the required fuel, and other factors.
These characteristics, in turn, affect the applications for which these cells are most suitable [11].
Five categories of fuel cells have received major efforts of research: [12]:

- Alkaline Fuel Cell (AFCs): they work with a low temperature aqueous alkaline electrolyte, a solution of potassium hydroxide (chemically, KOH) in water.They have the advantage of being able to start up easily from cold, and operate usually at 60-80 °C. At these temperatures, highly active catalysts are required, usually Nickel. Unfortunately they have several drawbacks such as the fact that AFCs are very sensitive to contaminants, in particular CO_2 which can poison the catalyst. Another point is the high alkalinity of the electrolyte can cause corrosion of certain materials leading to durability issues.

- Phosphoric Acid Fuel Cells (PAFCs): the electrolyte is a paper matrix saturated with phosphoric acid, transporting the hydrogen ions. The operating temperature is around 200 °C. The catalyst used is platinum, but at this temperature is sensitive to carbon monoxide decreasing the fuel cell's efficiency.

- Solid Oxide Fuel Cells (SOFCs): they are constructed entirely from solid-state materials, they use non-porous ceramic compound as the electrolyte. Are operated in the temperature range of 600-1000 °C. SOFC provide several advantages compared to other fuel cell types: they generate few problems with electrolyte management, they have the highest efficiencies of all fuel cells and for combined heat and power

applications internal reforming of hydrocarbon fuels is possible.

- Molten carbonate fuel cells (MCFCs): they are high-temperature fuel cells that use an electrolyte composed of a molten carbonate salt mixture suspended in a porous, chemically inert ceramic lithium aluminum oxide matrix. Because they operate at high temperatures of 650°C (roughly 1,200°F), non-precious metals, like nickel, can be used as catalysts at anode and cathode, reducing costs. The primary disadvantage of current MCFC technology is durability. The high temperatures at which these cells operate and the corrosive electrolyte used accelerate component breakdown and corrosion, decreasing cell life.
- Proton Exchange Membrane Fuel Cell (PEMFCs)

1.3.1. Polymer electrolyte membrane fuel cell

Polymer electrolyte membrane fuel cell (PEMFC) is an electrochemical device that converts the chemical energy of hydrogen and oxygen directly into electrical energy. Figure 1.4 shows a schematic of a PEM fuel cell.

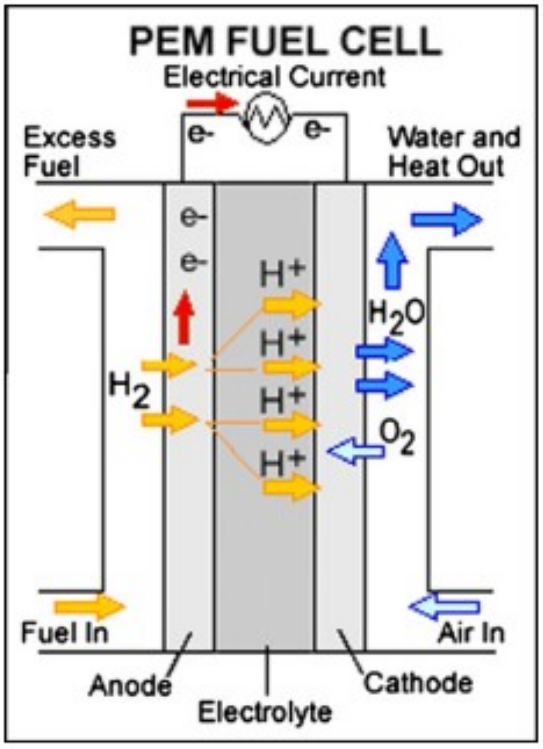

Figure 1.4: Schematic of a PEM fuel cell [10].

The core component of this fuel cell is a solid polymer electrolyte membrane. This membrane allows protons (hydrogen ions) to be transmitted from one face to the other while blocking electrons. There are two main electrochemical reactions that occur in this fuel cell. Once hydrogen (H_2) is supplied at the anode there's an oxidation process in which hydrogen molecules are split into protons (H^+) and electrons (e^-), the equation(1.10) represent the hydrogen oxidation reaction (HOR). The electrons are conducted through an external circuit generating electrical current and powering any connected devices or systems. The protons, as we already said, migrate to the cathode side passing through the membrane.
At the cathode side the reduction reaction takes place, the equation (1.11) is the oxygen reduction reaction (ORR). Indeed, air is supplied at the cathode side of the fuel cell, from air we get oxygen gas (O_2). Then, by combining oxygen molecules, protons, and electrons we produce water (H_2O), that with heat constitute the byproduct of the overall reaction.

$$Anode : H_2 \rightarrow 2H^+ + 2e^-, \tag{1.10}$$

$$Cathode : \frac{1}{2}O_2 + 2H^+ + 2e^- \rightarrow H_2O, \tag{1.11}$$

$$Overall : H_2 + \frac{1}{2}O_2 \rightarrow H_2O \tag{1.12}$$

Among the various types of fuel cells that we have seen in the antecedent section, proton exchange membrane fuel cell (PEMFC) has received great attentions and represent the most promising clean future energy source in recent years to replace conventional power generators. Indeed, they are characterized by remarkable aspects: high efficiency, high power density, low emissions,low operating temperature, and simple maintenance requirements. For all these reasons PEMFCs have great potential of application in industries, portable devices, automobiles and buildings, etc. as power generation devices or thermodynamic hybrid systems for specific requirements[23]. Nevertheless an effective widespread commercialization of PEM fuel cells has not come yet. Durability and costs are the main issues to address. Indeed, the noble metal-based catalysts are subject to corrosion over the long-term in the harsh conditions of proton exchange membrane fuel cell, this reduces significantly their lifetime. Moreover the typical catalyst of PEMFC is Platinum, it is a precious metal that increases the cost of the technology. Many improvements have been already done, mainly on the electrocatalyst part, but lots of improvements still awaiting. Mainly to meet competitive costs and durability criteria.

1.4. The European synchrotron (ESRF)

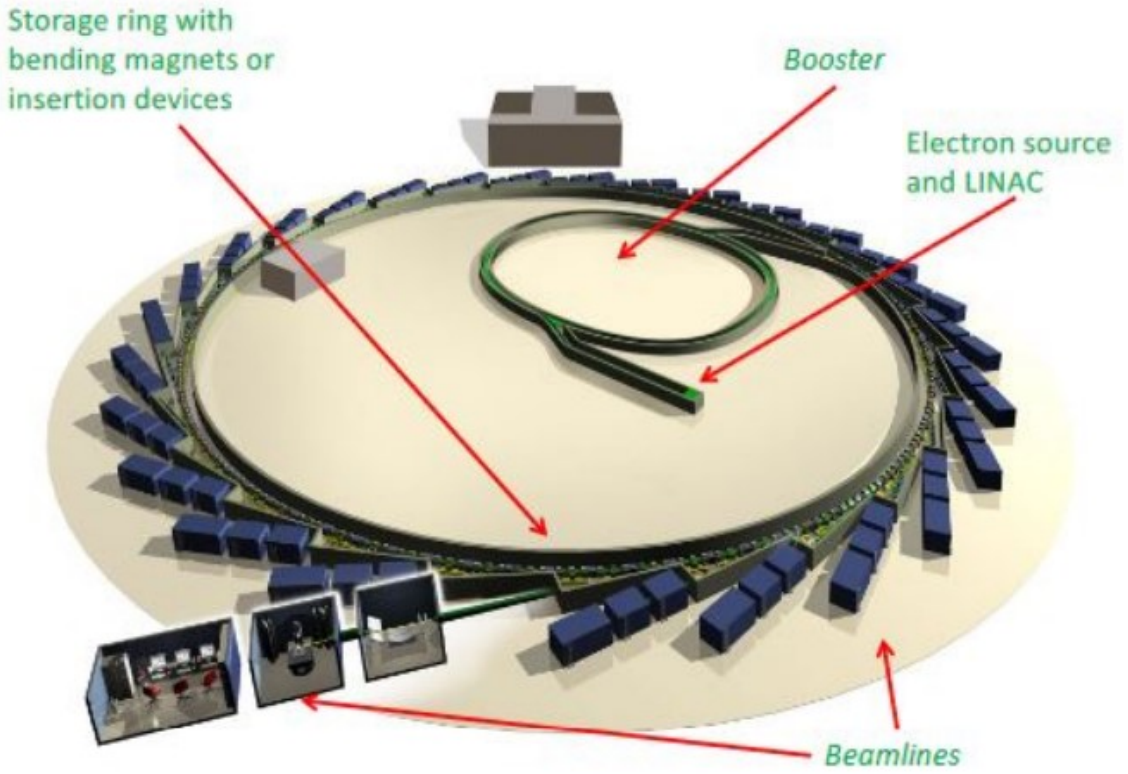

Figure 1.5: Schematic of the European Synchrotron of Radiation facility (ESRF) [14].

Founded in 1988 by twelve European countries, the ESRF is today the most powerful synchrotron radiation source of fourth generation in Europe for the production of high-flux photon beams by accelerating electrons to relativistic energies.
In figure 1.5 a schematic representation of the ring and the beamlines of the ESRF is shown.
Before emitting radiation, electrons undergo several processes of acceleration to reach their final energy. The electron beam is generated by an electron gun and then firstly accelerated up to energies of 200 MeV by a linear accelerator (LINAC). Then electron bunches are injected in a first accelerator of 300 meters of circumference, called booster, where they reach the maximum energy of 6 GeV. The electrons are then injected in a storage ring of 844 meters of circumference for X-ray radiation production. The ESRF storage ring can store a maximum current of 200 mA and is kept under ultrahigh vacuum (UHV) conditions to limit the interaction between electrons and the residual gas atoms. The storage ring is made of sequences of straight sections and curved sections.

The curved sections host bending magnets (BM), permanent magnets designed with the aim of deviating the overall trajectory of the electrons making them turning in a closed loop. Straight sections, instead, host insertion devices (ID), which consist of a sequence of dipole magnets of opposite polarities where the magnetic field (that can be varied by changing the gap between the poles) forces the electrons to oscillate around a straight trajectory, obtaining a highly collimated cone of emitted radiation.
There are two different types of IDs: wigglers and undulators. In an undulator the magnetic field is smaller compared to wigglers and so does the oscillations of the electrons, resulting in a further collimation of the beam [27, 28].
Figure 1.6 shows a schematic representation of the main sections of the storage ring. Actually the storage ring that has been just described has been largely renovated in the ESRF-EBS (Extremely Brilliant Source) upgrade project planned at ESRF (European Synchrotron Radiation Facility) in the period 2015-2022 [21]. This project aims to decrease the horizontal emittance and to improve the brilliance and coherence of the X-ray beams. Demanding specifications magnets have been designed for this project, in particular:

- *longitudinal gradient bending magnets*: unlike conventional bending magnets (dipoles), which bend particle trajectories only in the transverse (horizontal) plane, longitudinal gradient dipoles have the additional capability of bending particle trajectories in the longitudinal (vertical) plane.
- *quadrupole magnets*: these magnets have four poles arranged symmetrically around the beam axis and they can focus and converge the charged particle beams in one plane while simultaneously defocus and diverge them in the orthogonal plane.
- *sextupole magnets*: they have six poles arranged symmetrically around the beam axis and are designed to generate a magnetic field with a specific curvature that compensates for the nonlinearities in the main magnetic field.
- *octupoles magnets*: they have eight poles symmetrically arranged around the beam axis and are designed to compensate for third-order nonlinearities in the magnetic field.

The emitted radiation is finally collected by so-called beamlines that are installed along the storage ring, following the tangential direction of the beam. In those beamlines, different experimental set up are used for researching in many areas: engineering, physics, chemistry, earth science, biology and medicine.

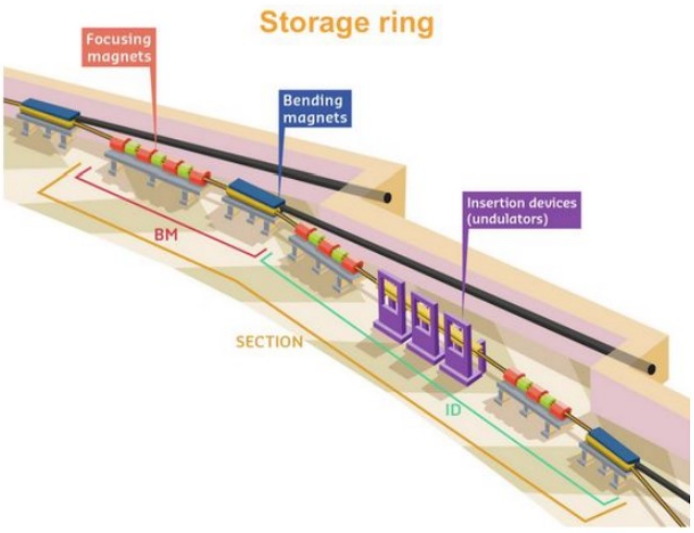

Figure 1.6: Schematic representation of the main sections of the storage ring: the bending magnet (BM) used for closing the overall trajectory of the electrons, the insertion device (ID) for the generation of synchrotron radiation, and focusing magnets [3].

An accelerated charge emits electromagnetic radiation, which in this particular case will be called synchrotron radiation. Furthermore, as a result of the radiation emission, the charges lose part of their kinetic energy. Thus, to restore the energy loss and to maintain a constant average energy along the ring, the electrons are further accelerated by straight devices called Radio-Frequency (RF) cavities. The electron passing through a RF cavity is kicked by the electric field to compensate the energy lost due to the radiation emission. However, this operation must be synchronized just with the electrons that have a lower energy. This synchronization implies that electrons cannot circulate along the ring as a continuous flow, but must form discrete bunches. This in turn implies that the synchrotron radiation is not continuous, but pulsed. Moreover, the number of circulating electrons decreases exponentially, because of the scattering with the residual gas atoms or due to a not perfect compensation of all the energy losses by the RF cavity. For that reason, when the current in the ring falls below a minimum acceptable level, new electrons are injected by the refilling procedure.

1.4.1. The synchrotron radiation

An accelerated charge emits electromagnetic radiation as a consequence of Maxwell's equations. In particular, synchrotron radiation is produced by electrons in the storage ring that move at relativistic speed. In the previous section has been introduced one type of insertion device used: the undulator, let's now discover the properties of the

synchrotron radiation it produces [40].
In figure 1.7 a schematic view of a planar undulator is showed. The undulator axis is along the direction of the beam (z direction) and the magnetic field points in the y direction (vertical).

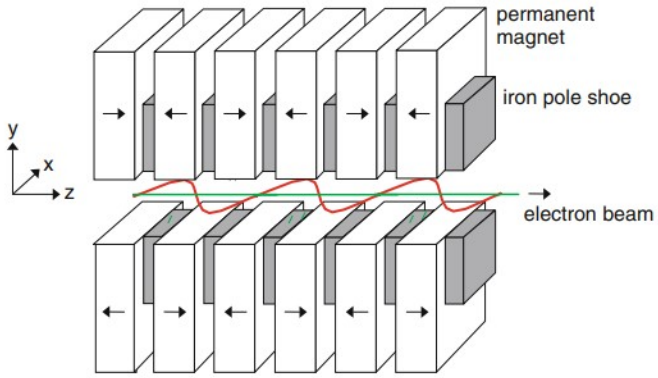

Figure 1.7: Schematic view of a planar undulator magnet with alternating polarity of the magnetic field and of the sine-like trajectory of the electrons. In the magnet shown here the field is produced by permanent magnets that are placed between iron pole shoes.

The magnetic field of a planar undulator is characterized by alternating poles, creating a periodic magnetic field pattern along the direction of electron motion. In particular, the magnetic field of an undulator is given by a sinusoidal function along the direction of the electron's motion:

$$B = -B_0 sin(k_u z) e_y, \tag{1.13}$$

where B_0 is the peak magnetic field strength, k_u is the wave number of the undulator and e_y is the unit vector in y direction. When moving electrons cross a magnetic field, their trajectory is modified following the Lorentz law:

$$\vec{F} = q_p \cdot \vec{v} \times \vec{B}, \tag{1.14}$$

where q_p is the charge of the particle, $\vec{v}$ is its velocity and $\vec{B}$ is the magnetic field. As we can notice the force due to the field is always perpendicular to both the direction of motion and to the direction of field.

From now on we will take into consideration two different reference frames for the moving electrons: i) the laboratory frame, whose plane is parallel to the plane of the ring and ii) the source frame, whose plane can be recognized as the inertial plane since moves along

with the electron at its constant speed v. Two important parameters are:

$$\gamma = (1 - \beta^2)^{-\frac{1}{2}}, \tag{1.15}$$

$$\beta = v/c, \tag{1.16}$$

By moving to the source frame we have to consider the relativistic mass of the electron, $m_0 = \gamma m$, where m_0 is the rest mass of the electron. So that the transverse acceleration by the Lorentz force is

$$\gamma m_e \dot{v} = -e\vec{v} \times \vec{B}, \tag{1.17}$$

The equation of motion is given by:

$$z(t) = \beta ct \tag{1.18}$$

$$x(z) = \frac{K}{\beta\gamma k_u} sin(k_u z) \tag{1.19}$$

where K is the undulator parameter

$$K = \frac{eB_0}{m_e c k_u} \tag{1.20}$$

The electron travels on the sine-like trajectory with a transverse velocity given by:

$$v_x(z) = \frac{Kc}{\gamma} cos(k_u z) \tag{1.21}$$

Due to the sinusoidal trajectory the z component of the velocity is not constant. The average longitudinal speed is

$$\overline{v_z} = \overline{\beta} c \tag{1.22}$$

By considering the undulator frequency as $\omega_u = \overline{\beta} c k_u$.The particle trajectory in second order is described by the equations:

$$z(t) = \overline{v_z} t - \frac{K^2}{8\gamma^2 k_u} sin(2\omega_u t), \tag{1.23}$$

$$x(z) = \frac{K}{\gamma k_u} sin(\omega_u t) \tag{1.24}$$

Let's now move to the moving coordinate system where electrons move at an average z

velocity

$$\overline{v_z} = \overline{\beta}c, \tag{1.25}$$

$$\overline{\gamma} = \frac{1}{\sqrt{1-\beta^2}} \simeq \frac{\gamma}{\sqrt{1+K^2/2}} \tag{1.26}$$

To move from source system to the other we will apply Lorentz transformations. In particular the Lorentz transformation from the moving system to the laboratory system reads:

$$t^* = \overline{\gamma}(t - \overline{\beta}z/c) \simeq \overline{\gamma}t(1-\overline{\beta^2}) = t/\overline{\gamma}, \tag{1.27}$$

$$x^* = x = \frac{K}{\gamma k_u} sin(\omega_u t), \tag{1.28}$$

$$z^* = \overline{\gamma}(z - \overline{\gamma}ct) \simeq -\frac{K^2}{8\gamma k_u}\sqrt{1+K^2/2}sin(2\omega_u t) \tag{1.29}$$

The electron orbit in the moving system is:

$$x^*(t^*) = asin(\omega^* t^*), \tag{1.30}$$

$$z^*(t^*) = -a\frac{K^2}{8\gamma k_u}\sqrt{1+K^2/2}sin(2\omega^* t^*) \tag{1.31}$$

with the amplitude $a = K/(\gamma k_u)$ and the frequency

$$\omega^* = \overline{\gamma}\omega_u = \overline{\gamma}\overline{\beta}ck_u \simeq \frac{\gamma c k_u}{\sqrt{1+K^2/2}} \tag{1.32}$$

The motion of electron is mainly a transverse harmonic oscillation with the frequency $\omega^* = \overline{\gamma}\omega_u$, the same frequency at which it emits dipole radiation in the moving system. The radiation power from an accelerated charge is given by the Larmor formula

$$P = \frac{q^2 a^2}{6\pi\epsilon_0 c^3} \tag{1.33}$$

Where P is the power of the radiation, q is the charge of the particle, a the acceleration of the charge, ϵ_0 the dielectric constant in vacuum and c the speed of light. Since we are considering an oscillating charge it follows that the value of the acceleration must be averaged over one period. Ignoring the longitudinal oscillation the acceleration has only an x component. The total radiation power in the moving system is:

$$P^* = \frac{e^2 c\gamma^2 K^2 k_u^2}{12\pi\epsilon_0(1+K^2/2)^2} \tag{1.34}$$

By transforming in the laboratory system:

$$P = \frac{e^4\gamma^2 B_0^2}{12\pi\epsilon_0 c m_e^2} = \frac{e^2 c\gamma^2 K^2 k_u^2}{12\pi\epsilon_0} \tag{1.35}$$

The radiation power formula shows that the radiation power P increases with the second power of the relativistic factor γ of the electron, making synchrotron radiation an excellent source of high-energy radiation.

When we consider a wave source moving with respect to the detector what we will have is that the radiation emission angle will be influenced by the relativistic motion of the electrons. In particular It is a general property of the radiation emitted by relativistic electrons in a magnetic field that at large distance most of the intensity is concentrated in a narrow cone of opening angle $1/\gamma$,The cone is centered around the instantaneous tangent to the particle trajectory. In the undulator magnet the electron describes a sinusoidal orbit and so the direction of the tangent varies, the maximum angle with respect to the axis is:

$$\theta_{max} \simeq \frac{K}{\beta\gamma} \simeq \frac{K}{\gamma} \tag{1.36}$$

If this directional variation is less than $1/\gamma$ the radiation field contributions from various sections of the trajectory overlap in space and interfere with each other. The consequence is that the radiation spectrum in forward direction is not continuous but composed of narrow spectral lines. Depending on how electrons are accelerated by means of bending magnets or insertion devices are used, different spectral distribution can be observed as we can see in figure 1.8.

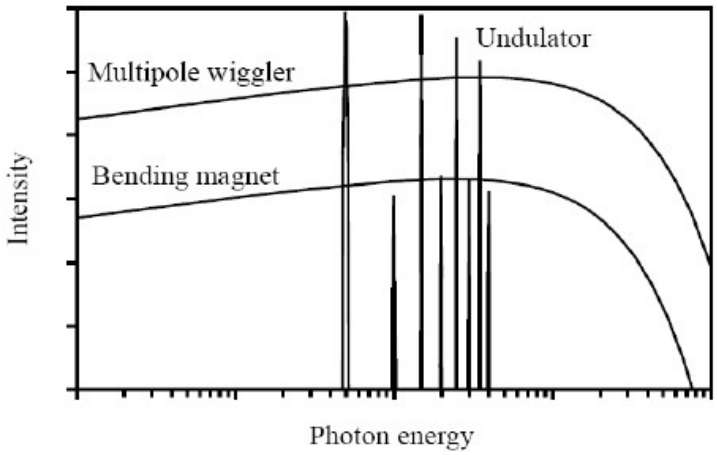

Figure 1.8: Spectral distribution of the radiation generated by a wiggler, a bending magnet and an undulator as a function of the photon energy. [18].

Their spectral distribution is entirely determined by the Lorentz contraction and by the Doppler effect. Again, to shift from source system to laboratory system let's consider the Lorentz transformations for momentum and energy are:

$$p_x = \gamma(p_x^* + \frac{v^2}{c}E^*), \tag{1.37}$$

$$p_y = p_y^*, \tag{1.38}$$

$$E = \gamma(E^* + vp_x^*), \tag{1.39}$$

where x identifies the direction tangent to the orbit ans y the perpendicular one. When a photon is emitted by the source and travels along the orbit it has $E^* = \hbar\omega_u^*$, $p_x^* = \hbar\omega_u/c$, $p_y^* = 0$. By applying those simple transformations :

$$E = \gamma(\hbar\omega_u^* + v\frac{\hbar\omega_u^*}{c}) = \hbar\omega_u^*\gamma(1+\beta), \tag{1.40}$$

So that for relativistic speed one can estimate Doppler shift as $\omega_u \simeq 2\gamma\omega_u^*$ that in turn will result in a strong reduction of photon wavelength as measured in laboratory frame frame:

$$\lambda_u \simeq \frac{\lambda_u^*}{2\gamma} \tag{1.41}$$

An electron moving along an undulator of period Δx (i.e. the distance between couples of opposite permanent magnets) causes the emission of synchrotron radiation with a wavelength that depends on the frame we are considering. Indeed we know that due to relativistic velocity in the electron frame its period is contracted to $\Delta x/\gamma$ and the magnetic field becomes a transverse electric field, so that the electron oscillation period will correspond to the wavelength of the emitted radiation in S, $\lambda_u^* = \Delta x/\gamma$. We also know that the photon wavelenght in the frame L is also Doppler-shifted by a factor 2γ, so that:

$$\lambda_u \simeq \frac{\lambda_u^*}{2\gamma} = \frac{\Delta x}{2\gamma^2} \tag{1.42}$$

By assuming that the light is detected at an angle θ_L from the axis:

$$\lambda_u = \frac{\Delta x}{2\gamma^2}(1+\gamma^2\theta_L^2) \tag{1.43}$$

So that the undulator emission can be seen as the coherent superposition of different photons emitted by N sources, where N are the number of couple magnets, all characterized

by short wavelength. And the associated resolving power is:

$$\frac{\lambda_u}{\Delta\lambda_u} = mN \tag{1.44}$$

That means that the undulator spectrum is made of several narrow peaks for each of the harmonics whose angular spread is further narrowed by increasing N. This results in a extreme angular collimation.

1.5. The ID31 - High-Energy Beamline For Buried Interface Structure and Materials Processing

ID31 is a dedicated beamline at the European Source Radiation Facility for interface and materials processing studies using high energy x-rays, [4][39].
It has been designed with the aim of supporting innovative works with the use of hard X-ray characterisation techniques including reflectivity, wide and small angle diffraction (both in transmission and grazing incidence geometry), imaging methods, auxiliary techniques, coupled with a great versatility in choosing beam sizes, energy and energy-band.
This beamline was born as an evolution of ID15 with the aim of providing high energy x-rays at the ESRF and in Europe in general, with an x-ray beam characterized by a bandwidth and a spot size that can be chosen as freely as possible.
The x-ray source should provide the highest possible intensity in the energy range of 20 to 150keV. So the optimum x-ray source is an in-vacuum cryo-cooled undulator with 14.5mm period, U14. So, ID31 is an undulator beamline. In the following, figure 1.9, the brightness of U14 compared to the U22 that was used at ID15 is shown.

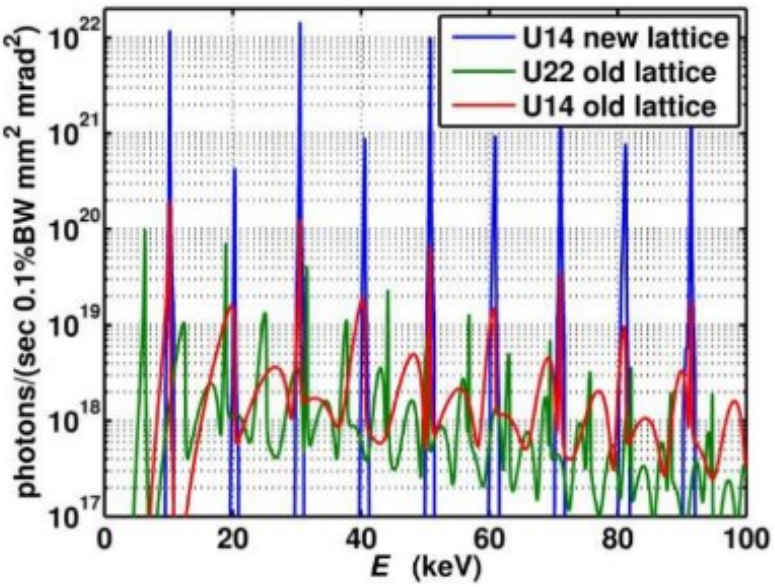

Figure 1.9: The brightness of U14 compared to the U22 currently used at ID15. The brightness is given also for the new lattice.). [39].

The structure of the beamline, after the radiation source, can be described with the identification of three main zones in which the beam is sent:

- The *optical hutch*: close to the ring, here are located several optical devices used to

to filter and focus the beam.

- The *experimental hutch*: is where the experiment takes place, all the detectors used for measuring and recording information about the radiation-matter interaction are located in this part.Because of the strong X-ray beam, this hutch is automatically locked during operation for safety reasons.
- The *control cabin*: where researchers can monitor the experiment and analyze the obtained data

The general layout of the beamline is showed in the figure 1.10.

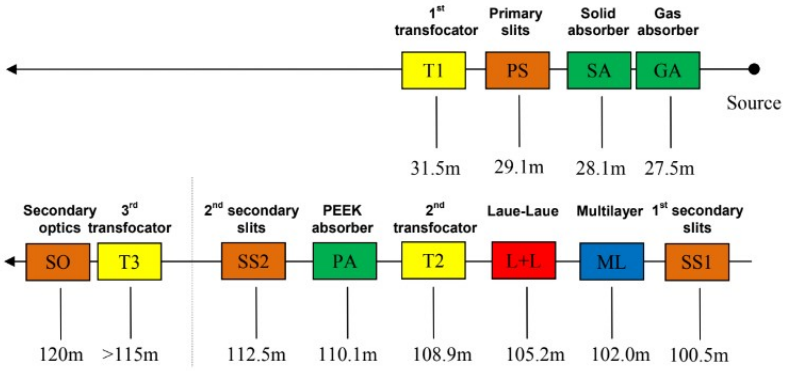

Figure 1.10: General optics layout. The upper panel shows the components in OH1 whilst the lower panel shows the components in OH2 and EH (3rd transfocator and secondary optics). [39].

The focusing optics consist of three transfocators. In the first optical hutch (OH1) a white beam transfocator(T1) to condense the incident beam when very intense beams with medium range spot sizes are needed. In the second optical hutch (OH2) the beam gets monochromatic thanks to multilayer or Laue-Laue monochromator, the second transfocator (T2) to focus a beam with low divergence to the sample or to detector. Finally, a monochromatic beam transfocator or KB optics in the experimental hutch to provide sub-micron beams.

1.5.1. High Energy X-Ray Diffraction

X-ray diffraction (XRD) is a technique extensively used for the characterization of materials. It is primarily employed as a bulk sensitive analytical method used to determine crystal structure, crystallite size and strain for non amorphous materials. A crystal is a

solid material whose constituents (such as atoms, molecules, or ions) are arranged in a highly ordered microscopic structure, forming a crystal lattice that extends in all directions [36].
The investigated sample can be regarded as a collection of a huge number of scatterers, each of them, when stimulated by the incident x-ray radiation, generates a spherical wave. The incident wave is characterized by a wave vector k_i while the wave scattered at an angle θ has wave vector k_s. An elastic scattering implies $|k_s| = |k_i|$ from this we derive that the magnitude of the scattering vector is $q = 2k_i = \sin\theta$ where $k_i = 2\pi/\lambda$ and λ is the wavelength of the impinging radiation.
The spherical waves produced by the atoms of the crystal give rise to constructive interference only in some specific directions determined by the very well known Bragg's law:

$$n\lambda = 2d\sin\theta \tag{1.45}$$

where d is the spacing between diffracting planes, θ is the incident angle, n is any integer, and λ is the wavelength of the beam.

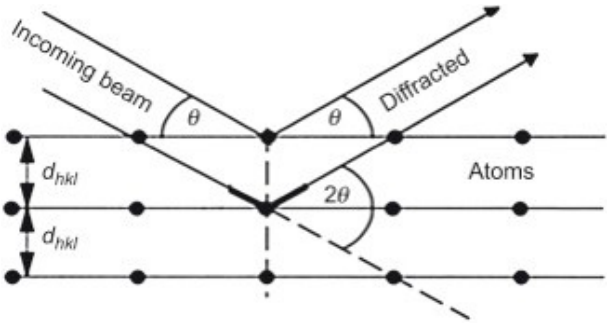

Figure 1.11: The incoming beam (coming from upper left) impinging with θ angles causes each scatterer to re-radiate a small portion of its intensity as a spherical wave. If the atoms in the crystal are arranged in planes separated by d, these spherical waves will interfere constructively only in directions where their path-length difference equals an integer multiple of the wavelength. In that case, part of the incoming beam is deflected by an angle 2θ, producing a reflection spot in the diffraction pattern [30], [17]

.

Using synchrotron x-rays is convenient since they allow better sensitivity and resolution of diffraction peaks than conventional laboratory XRD. This is due to the unique properties of synchrotron radiation that we have seen in section 1.4.1. Moreover, the high-energy x-rays characterized by energies in the range of 20-150 keV allow the experience of other unique advantages [4]. Indeed, due to a strongly reduced photo absorption cross section is possible to reduce the damage of the sample due to the beam. Also, there's the possibility

of wide access to reciprocal space and mapping of regions over several Brillouin zones. Here in the following a sketch of the setup at ID31, fig.1.12. The x-rays reach the PEMFC and produce diffraction patterns on the detector. The use of a 2D detector makes this setup very efficient at high energies, a more specific explanation is given in section 2.2.3.

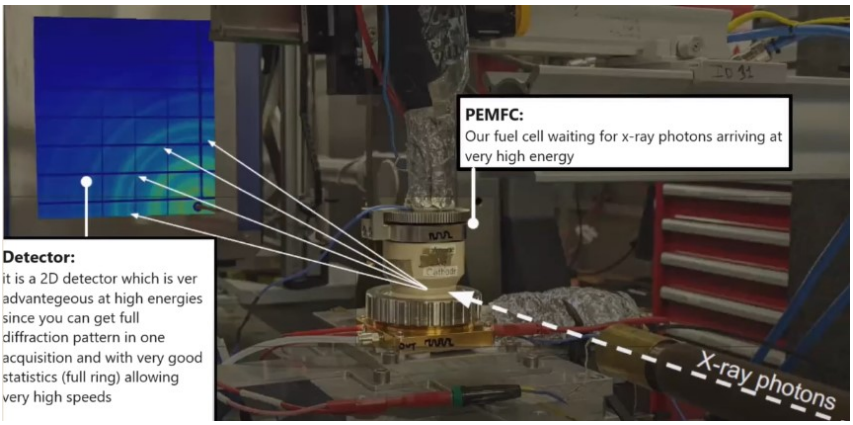

Figure 1.12: A sketch of the setup at ID31 [16].

1.6. Outline of the thesis

The outline of this manuscript is as follow:

- Chapter 2 presents the methods and materials used in the study. At the beginning the design and the assembly of the PEMFC used in this work is described. Then the experimental techniques are explained. Particular attention is given to a profound description of the sample preparation, more details of the XRD are given coupled with a full explanation of the detectors used. The electrochemical techniques adopted at the scope of this study are introduced and explained. Following the methods used for the data analysis are showed. In particular the azimuthal integration, the rietveld analysis, Topas software and the analysis in python are descripted.
- Chapter 3 presents all the results obtained from the calculation and experimental measurements described in the previous chapter.
- Chapter 4 presents an interpretation to the results of this study, also an explanation of their significance will be given together with some possible improvement in the method and further studies.
- Chapter 5 presents the main conclusions of the work

2 | Material and Methods

2.1. Design of the Proton-Exchange Membrane Fuel Cell

The Proton-Exchange Membrane Fuel Cell (PEMFC) has been already largely discussed in section 1.3.1, here we describe the design of the proton exchange membrane hydrogen fuel cell adopted in the experiment [35].
The cell body, shown in Fig. 2.1, was machined from polyether ether ketone (PEEK). The two flowfield plates are held together by the cell body, without metallic posts which would obstruct the beampath during cell rotation. A low profile threaded aluminum ring mounts the cell body against the bottom heatsink. This ring partially attenuates the lower part of the 2D diffraction pattern and this needs to be accounted for during the data analysis. An internal thread inside the upper housing allows compression of the two flow fields against the sample with controllable, homogeneously distributed mechanical pressure. The graphite flow fields are attached to brass and copper heat sinks with embedded thermocouples and cartridge heaters. A parallel flow field design was selected such that X-rays can transit the length of the cell without passing through thick layers of graphite. A very small flow field pitch (1 mm) minimizes the mechanical distortion to the PEMFC and keeps the sample flat, improving the quality of the alignement.

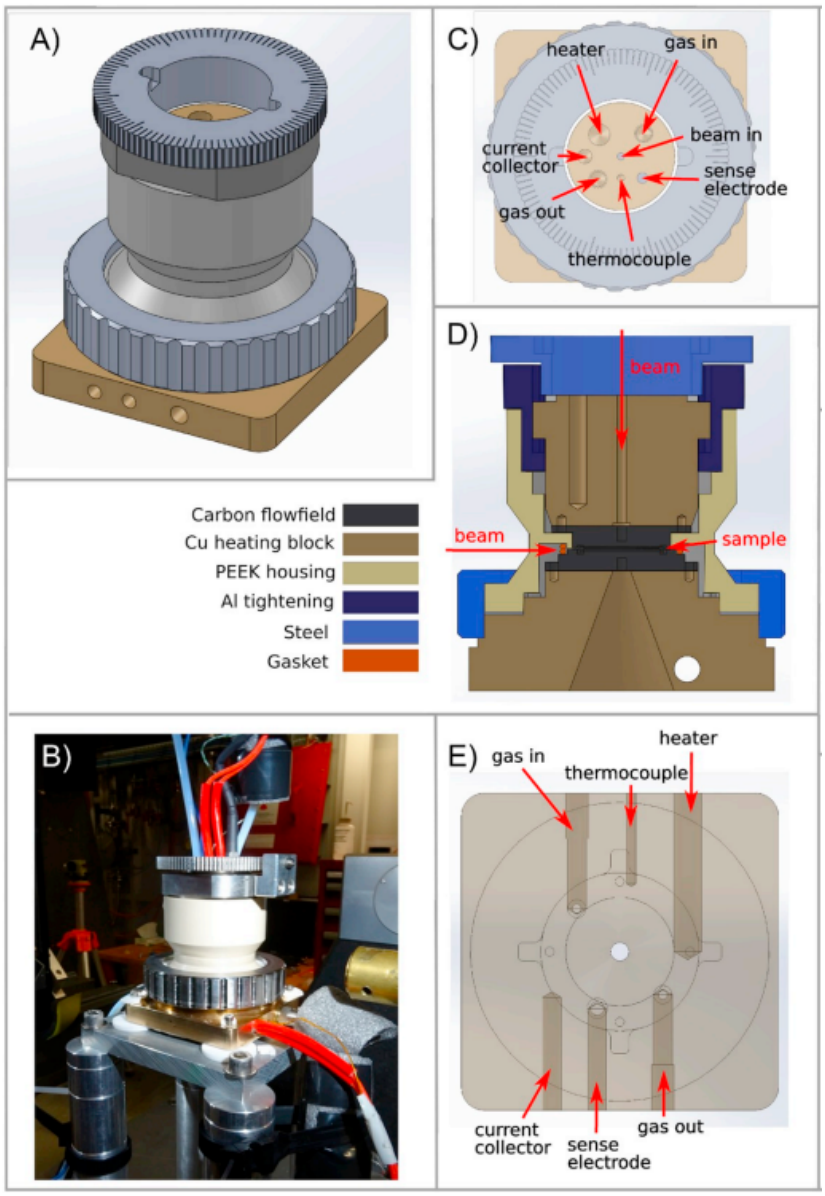

Figure 2.1: 3D rendering of the 5 cm2 PEM fuel cell (A). Cell configured on beamline (B). Top (C), side (D) and bottom (E) view of the cell with marked cell connection details and beam directions for two possible measurement geometries [35].

2.1.1. Design of the Membrane Electrode Assembly

The Membrane Electrode Assembly (MEA) is the core component of a fuel cell and it consists of several layers of materials that work together to facilitate electrochemical reactions [20].We can see the schematic structure of the MEA in Fig. 2.2. The heart of the MEA is the PEM, made of Nafion 112, it is a thin, 125 μm, and solide electrolyte that allows the passage of protons while blocking the flow of electrons. For this study

the MEA was prepared by cutting CCM, catalyst coated membrane, into $25mm^2$ piece and laminating it into a larger Mylar frame. On one side of the CCM there is the anode catalyst layer and on the other side there's the cathode catalyst layer, those two are both consisting of platinum nanoparticles supported on carbon. Indeed, the anode is carbon-supported Pt with 0.079 mgPt/cm2 loading, the cathode, 0.187 mgPt/cm2 with the average nanoparticle size determined by XRD of the CCM of 2.9 nm. On both side of the MEA we aligned SGL 22BB GDL, gas diffusion layer, which is a porous material that provide pathways for the reactant gases (hydrogen and oxygen) to reach the catalyst layers. Kapton subgasketing surrounding the active area of the MEA was used to to prevent gas leakage and maintain proper separation between the anode and cathode compartments [38][35].

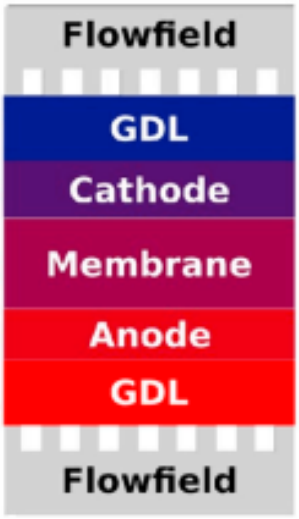

Figure 2.2: Schematic representation of the MEA structure [35].

2.2. Experimental techniques to study electrode kinetics

Let's now see the steps done during the experiment in order to carry out the study.

2.2.1. Sample preparation

The first step is preparing the sample, actually at least 4 MEA samples have been prepared following the method given in section 2.1.1.
When the sample is appropriately prepared it is mounted in the fuel cell described in section 2.1. SP240 Biologic potentiostat was connected in the 4 electrodes setup. Voltage

cables were connected directly to graphite flow fields, and the current was collected from the adjacent copper blocks. Once the fuel cell is connected to the Test Station then the gas distribution, humidification and potentiostat can be controlled remotely. In the following figure it is possible to see how the fuel cell looks like from the point of view of the detector, hoping the detector has better resolution than this.

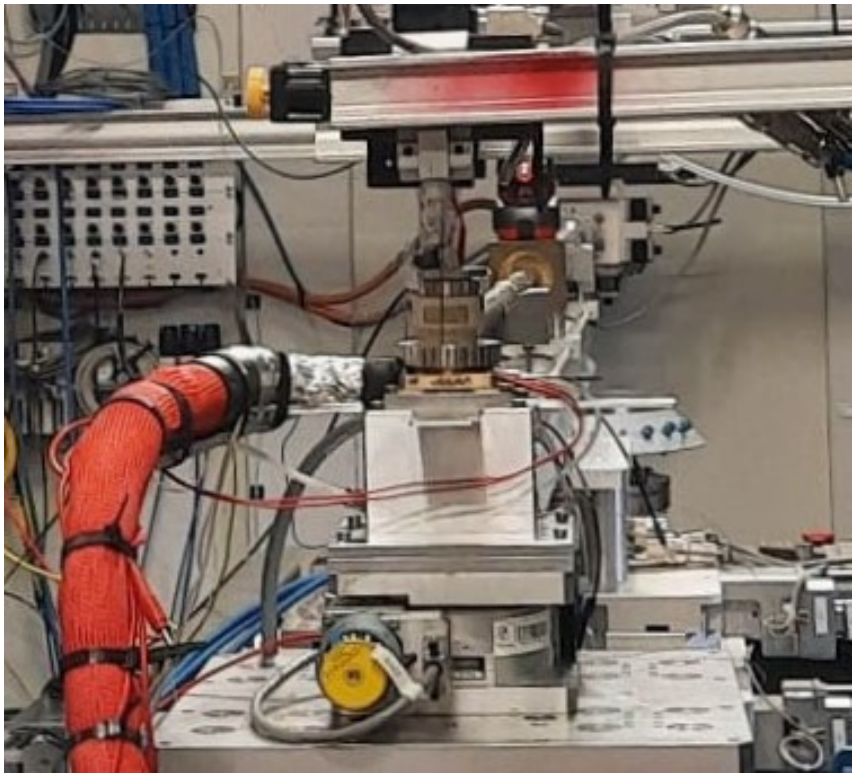

Figure 2.3: Fuel cell mounted in ID31.

To ensure that the X-rays hit the desired region of interest on the sample, a proper alignment of the sample with respect to the incoming X-ray beam has to be done. Thanks to a remote control it is possible to modify the position of the cell with translations, rotations, or tilts of the motors. As we can see from the following pictures, different cameras pointing to the FC help to visualize the situation in the experimental hutch.

(a) (b)

Figure 2.4: Pictures from the cameras used for the alignment of the sample.

This alignment is typically performed at a relatively low X-ray flux to avoid sample damage. In particular in our case, the interest is on finding where is the cathode, so that the possible spots where sending x-rays are identified. In the figure 2.5 we have an example of the plots that are followed to do the alignment. We look for the platinum signal, which will come both from the cathode and the anode, in particular the one coming from the cathode will be higher in intensity since it is more loaded on Pt. All the plots present in figure 2.5 correspond to Pt profiles, but the yellow, green and pink curves are due to a misaligned cell. The goal, indeed, is to have as separated peaks as possible. Once a good Pt profile is obtained, the red one for example, the motors position is modified so that the beam will point to the cathode catalyst layer.

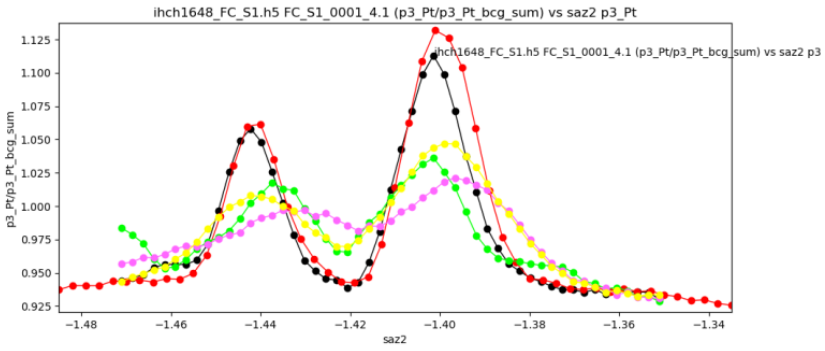

Figure 2.5: Example of alignment plot: the yellow one seems the profile that resembles the most to Platinum.

Once this alignment procedure has finished sample conditioning must be done.
Sample conditioning is done to prepare the sample for the analysis and to do experimentation in the best possible state to obtain accurate and reliable data. At this aim a Test

Station is used in order to evaluate the performance of the fuel cell. A custom control software is available in ID31 in order control the inputs and outputs of the test station, and consequently of the FC. As we can see in figure 2.6, different parameters can be controlled. In our case, for the sample conditioning, O_2 is sent to the cathode and H_2 to the anode and we run it for 30min at constant voltage, 0.6 V. The temperature of the cell is set at 75° and relative humidity is 100/100 sccm. In PEMFCs, maintaining the appropriate relative humidity is crucial. The membrane requires a certain level of water content to conduct protons effectively. If the relative humidity is too low, the PEM can dry out, leading to decreased ionic conductivity and reduced performance. Conversely, if the relative humidity is too high, excess water can accumulate, leading to flooding and limiting reactant flow through the porous electrodes. Another parameter that is taken into consideration is the Control Current or CCA flow, meaning the amount of electrical current flowing through the fuel cell. Since a current of 120 mA is registered this means CCA $<$ 0.5 A/cm2.

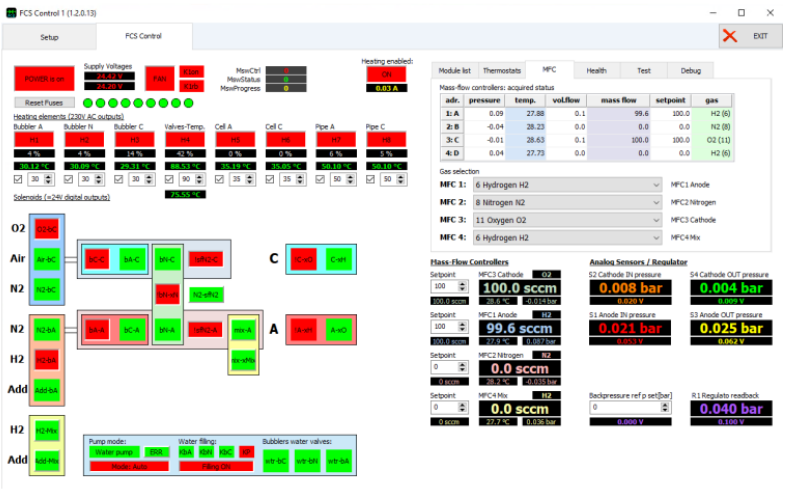

Figure 2.6: Example of the screen of the custom control software.

2.2.2. Powder Diffraction

Platinum nanoparticles undergoing different electrochemical processes are studied thanks to XRD technique. X-ray photons with a high kinetic energy (77 keV) are employed since they are enable to penetrate the complicated sample environments necessary for electrochemical experiments. Then, thanks to the use of 2D detectors, see section 2.2.3, one can scan large parts of reciprocal space within a single detector image.
For what concerns the choice of nanoparticles, that is connected to the fact that their very small size leads surface processes to significantly affect the bulk properties of such

materials and can be studied even with bulk sensitive X-ray diffraction technique.
As we have already seen in section 1.5.1, by picturing a crystal as containing planes identified by Miller indices (hkl), then the Bragg's law applies, eq.1.45, giving the angle of constructively scattered intensity. For a single crystal, we get beams of diffracted intensity in specific directions when Bragg's law is satisfied.
In our case we have a powdered sample, that consist of many small crystallites randomly orientated. This means that for a certain d_i spacing of the planes, there will be a certain number of crystallites having the correct orientation to produce constructive diffraction, all together those diffracted beams are added into concentric cones each of which corresponds to different spacing. These cones would intersect a flat detector surface as circles, known as Debye-Scherrer rings, these are a characteristic feature of diffraction obtained from powdered or polycrystalline materials.

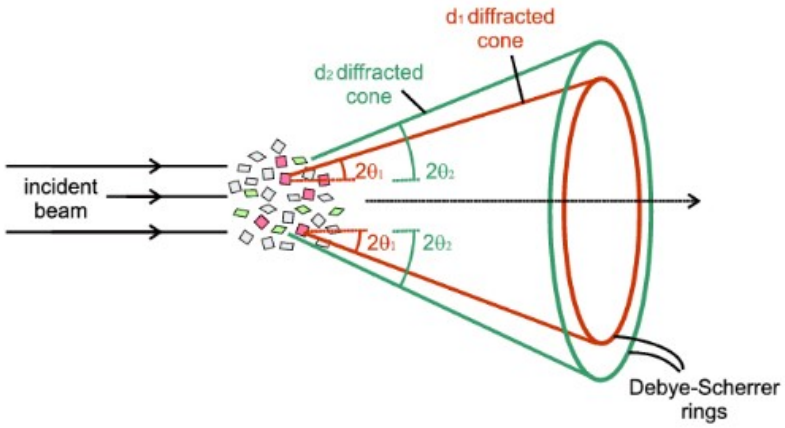

Figure 2.7: Diffraction of a powdered sample leads to cones of diffracted intensity which are intersected as circles on a 2D detector surface, with each circle corresponding to an individual or overlapped set of hkl reflections [28] [15].

For each discrete diffraction angle 2θ the number of reflections is measured (in counts) by the detector. The position and spacing of the Debye-Scherrer rings provide valuable information about the crystalline structure of the material.

2.2.3. Detection system

To study the above phenomena two detectors are used.

- *CCD Si based detector PCO DiMAX*: using a special fluorescence screen coupled with the ultra fast CCD (Charge-Coupled Device) Si based detector (PCO DiMAX) we are able to measure the diffraction patterns at very high speeds (20kHz). The

incident X-ray beam is directed at a crystalline sample, the interaction between the X-rays and the electrons in the sample causes the X-rays to scatter in various directions. The scattered X-rays hit the fluorescence screen. This fluorescence surface will emit visible light once it is exposed to X-rays. Then, the PCO DiMAX camera with its CCD sensor, will detect the visible light produced by the fluorescence screen. Such new setup is a new instrumental development allowing access to time-scales not feasible before in diffraction experiments. The evolution of the system can be captured with high temporal resolution. A feasibility study carried in ID31 shows that rates close to the single bunch detection might be possible.

- *Pilatus 3X CdTe 2 M hybrid photoncounting area detector[6]*: this detector is a powerful tool for studying dynamic processes, fast reactions, and transient phenomena with high temporal resolution. Fast data acquisition it's possible thanks to a hybrid pixel technology, where each pixel in the detector has its own readout electronics. This allows for parallel readout of multiple pixels simultaneously. Also the CdTe sensor in the detector directly detects X-ray photons, so that rapid detection is possible without the need for additional conversion layers. In our case with this detector we measured at 200Hz.

2.2.4. Electrochemical techniques

In electrochemical kinetics, the electrode potential is the most important variable that is controlled by the experimentalist, and the current is usually measured as the response. Thanks to the use of a potentiostat, in our case BioLogic SP-240 potentiostat [8], one can measure and control the voltage difference between the working electrode and the reference electrode, which has a constant potential. In particular we used the potentiostat in the potentiostatic mode that means that the potential of the working electrode is held at a constant value while the resulting current is measured as a function of time. The remote control of the potentiostat is possible thanks to EC-Lab which is the BioLogic's benchmark control/analysis software [8].
In this scenario is important to take into consideration one quantity that influences the measurement accuracy: the ohmic drop [8]. With this term, in electrochemistry, it is indicated the potential induced by the current flow through the electrolyte (with an inherent resistance) or any other homogenously resistive components such as surface films or connectors. By identifying the ohmic drop with $R_\Omega I$, and $V(t)$ with the potential seen by the electrode and $E(t)$ as the desired potential, we have $V(t) = E(t) + R_\Omega I$. In order to reduce the ohmic potential drop a solution is to use fuel cell, in which we have the reference electrode as close as possible to the working electrode. Also, compensations

techniques are used to determine and correct the ohmic drop. In our case to obtain the right value of the ohmic drop we measure the cell resistance by electrochemical impedance spectroscopy (EIS) [2], which is a valuable tool for characterizing fuel cell behavior.
An impedance measurement system relies on alternative current techniques so that the response of the system to a potential or current sinusoidal perturbation is studied as a function of the frequency. EIS measurements should be made on a system that is linear and steady-state. The linear behavior is assured by applying a signal with a small amplitude. In our study a perturbation of the potential is applied. The response of this electrical signal is represented in a Nyquist plot. In this type of plot the real part of impedance is on the x-axis and the imaginary part on the y-axis. By measuring the real part of the impedance, the total cell resistance (Ohmic resistance) of the fuel cell is obtained. The value of the resistance to be compensated can be entered manually in the compensation mode of potentiostat.
Once determined the fuel cell resistance the rates and mechanisms of electrochemical reactions occurring at electrodes are studied thanks to two techniques [41]:

- *Potential Step (PS)*: it is a transient technique since at the starting point the system is at equilibrium and after the perturbation it returns back to the equilibrium state. The working electrode is held at a stable initial potential for a period of time necessary to establish equilibrium, let's say this happens at time $t<0$. Then, at a time $t=0$, a potential step of the desired magnitude is applied with the aid of a potentiostat and the current transient is recorded. In the following table 2.1, a sum up of all the different potential steps done during the experiment is showed. Every step has been done following the same procedure: hold the potential at 0.35V for 1.2s then go for 5s to the potential registered in the first column of table2.1 and then back to 0.35V for 10 s. The second and third columns of table2.1 show the detector used. In particular the second column refers to the use of Pilatus 3X CdTe 2 M hybrid photoncounting area detector, the third to the use of CCD Si based detector PCO DiMAX.

	Voltage (V)	Pilatus	Fast Detector
S1-steps_12	1.2	x	
S1-steps_13	1.2		x
S1-steps_14	1.2		x
S1-steps_15	0.9	x	
S1-steps_16	0.9		x
S1-steps_17	0.8	x	
S1-steps_18	0.8	x	
S1-steps_19	0.8		x
S1-steps_20	0.7	x	
S1-steps_21	0.7		x
S1-steps_22	0.6	x	
S1-steps_23	0.6		x
S1-steps_24	0.5	x	
S1-steps_25	0.5		x
S1-steps_26	0.1	x	
S1-steps_27	0.1		x

Table 2.1: List of the potential steps done during the experiment.

- *Cyclic Voltammetry (CV)*: the perturbation is periodic, and after an initial, transitory period the response will be periodic as well. The potential of the working electrode is varied linearly with time between two turning points. The potential is swept in one direction, forward scan, from an initial potential to a final potential and then reversed back to the initial potential, reverse scan. The potential sweep rate, i.e., the speed at which the potential is changed, is controlled during the experiment, the variation of the frequency of the perturbation is the key to studying processes occurring at different velocities. In the following table 2.2, a sum up of all the different Cyclic Voltammetry done is showed. Every CV has been done following the same procedure: go from 0.1V to 1.2V in a scan rate registered in the first column of table2.2 for a minimum of 2 cycles. The second and third columns of table2.2 show the detector used. In particular the second column refers to the use of Pilatus 3X CdTe 2 M hybrid photoncounting area detector, the third to the use of CCD Si based detector PCO DiMAX.

	Scan rate	Pilatus	Fast Detector
S1-CV_19	5V/s		x
S1-CV_20	3V/s		x
S1-CV_21	1V/s		x
S1-CV_22	700mV/s	x	
S1-CV_23	500mV/s	x	
S1-CV_24	200mV/s	x	
S1-CV_26	100mV/s	x	
S1-CV_27	50mV/s	x	

Table 2.2: List of the cyclic voltammetry done during the experiment.

2.3. Data analysis protocol

Before introducing the chosen analysis method, let me just mention that in ESRF the experiment control system used to run the beamlines after the ESRF Extremely Brilliant Source upgrade (ESRF-EBS) is BLISS (BeamLine Instrumentation Support Software) [1]. Provided with a Python programming language BLISS allows to control the experimental parameters, such as beamline settings, sample positioning, and data acquisition conditions. The software enables real-time data collection during the experiment.

2.3.1. Azimuthal Integration

At this point of the dissertation is probably well understood that hitting a crystalline sample by X-rays will produce a scattered radiation that results in a diffraction pattern, which consists of spots or peaks on a two-dimensional detector. But, for the purpose of extracting quantitative information from the diffraction pattern an azimuthal integration is needed. Performing an azimuthal integration means summing up the intensities of diffraction peaks along concentric rings as a function of azimuthal angle, which is the angle of rotation around the direction of the incident beam. In order to accomplish the goal of reducing the raw diffraction data into a one-dimensional intensity profile as a function of the scattering angle, 2θ, the software package pyFAI is used [13].
PyFAI is implemented in Python programming language and it is a valuable tool to perform azimuthal integration of diffraction data. Indeed, it is possible to convert the data coming from Cartesian space (x,y) to polar space $(2\theta, \chi)$, also a calibration graphical interface is normally used to optimize the geometry of the experiment using the Debye-

Scherrer rings of a reference sample, in our case CeO_2.
Once the data are integrated, we can proceed working on those data with TOPAS software, based on Rietveld analysis, and Python. In the following chapters a detailed explanation will be given.

2.3.2. Rietveld analysis

The positions and intensities of the diffracted peaks obtained from X-ray diffraction data of a powdered sample give valuable informations related to the crystal structure of the material we are studying. With this aim in this study the Rietveld refinement method is used [28], based on comparing the measured diffraction pattern with a calculated pattern based on a structural model.
The starting point is to calculate a diffraction pattern from initial structural model, of Platinum in our case. Indeed from this model we can fit informations about the position of the atoms, their thermal vibrations, and other relevant crystallographic parameters.
The calculated pattern is then convoluted with a profile function to account for instrumental effects and sample characteristics. So, let the calculated intensity at diffraction angle $2\theta_i$ be $y_{calc,i}$ and let $y_{obs,i}$ be the observed intensity at diffraction angle $2\theta_i$, then the goal is to minimize the difference between the two:

$$\sum_{i=1}^{N} w_i (y_{obs,i} - y_{calc,i})^2 \tag{2.1}$$

It can be considered an example of solving an inverse problem in crystallography. Indeed, Rietveld analysis involves determining the parameters that produced the observed results. Essentially, it's about finding the crystal structure that produced the given diffraction pattern. The way of proceeding is following an iterative process that adjusts the parameters of the crystal structure model to minimize the difference between the calculated diffraction pattern and the experimental data, see 2.1. The process is normally followed by checking that the weighted profile R factor tends to low values, where:

$$R_{wp} = \sqrt{\frac{\sum_{i=1}^{N} w_i (y_{obs,i} - y_{calc,i})^2}{\sum_{i=1}^{N} w_i y_{obs,i}^2}} \tag{2.2}$$

And checking that the quantity named the goodness of fit (GoF) tends to 1:

$$GoF = \sqrt{\frac{\sum_{i=1}^{N} w_i (y_{obs,i} - y_{calc,i})^2}{N - P}} \tag{2.3}$$

where N is the number of data points and P the number of parameters.

2.3.3. TOPAS

Once the theory behind the analysis of the data is understood is important to find a software thanks to which it is possible to handle with the huge quantity of data collected thanks to fast acquisition.
Topas is the answer, or better saying: Total Optimization from Powder Patterns using the Alternating least squares method. This powerful suite of software, written by Alan Coelho, allows the analysis of powder diffraction data by performing Rietveld refinement[7]. In order to access all the features of TOPAS an open-source text editor is used: JEdit. Through JEdit it is possible to edit a text based input file, as we can see in figure 2.8.

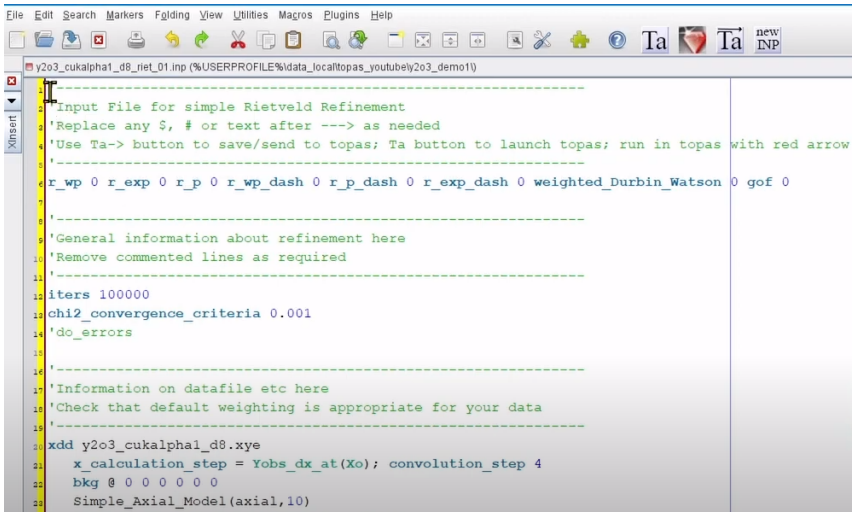

Figure 2.8: Screenshot of an .inp file opened in JEdit.

This input file has as input the integrated data saved in files with .xye extension, each of which corresponds to a certain electrochemical condition at certain time. A dedicated analysis will be carried out for every potential step (PS) and cyclic voltammetry (CV) registered in the tables 2.1 and 2.2 performed with Pilatus detector. Since a quantity of frames superior to 2000 for each PS or CV have to be analyzed, the only way to handle with all these data is to perform a sequential refinement.
The power of JEdit is indeed this one, it is through the use of macros that we can customize our analysis. Macros allow to perform batch analysis, that means to process multiple datasets sequentially, saving the results for further analysis . The task is to custom the input file so that it has the right parameters and macros able to extract information from the diffraction data. From section 2.3.2, we understood that Rietveld refinement

needs a structural model to refer to in order to construct a calculated diffraction pattern. For this reason a Platinum CIF file (Crystallographic Information File) is uploaded, it contains the atomic and crystallographic information of a crystal structure. Then, initial parameters defining the scale and lattice parameter have to be defined. And so on and so forth defining all the parameters we would like to be refined till we are ready to launch TOPAS, load the .inp file and start the analysis. Once the refinement is completed an output file will be automatically produced and saved in the desired directory, it will contain all the results of the analysis.

2.3.4. Python

Once the refined parameters are obtained thanks to the amazing power of TOPAS, time has arrived to extrapolate valuable informations from those data. Who better than Python could be addressed for this scope?
A dedicated script for every PS and CV is written. In both cases there was the need to combine the data obtained from the electrochemistry and the x-rays, in order to do so it is necessary to synchronize them through the epoch. Data from the potentiostat are obtained from a BioLogic.MPRfile, this file gives us informations about the time, the relative potential applied and the intensity registered. Data from x-rays are those coming from the output file of TOPAS. Then two different type of studying were carried out.

- *Potential Step script*: In order to model the change in value both of the lattice parameter (LP) and the scale, an exponential trend is chosen. The function curve_fit form the scipy.optimize package is used in the interest of finding the parameters describing the exponential trend.

- *Cyclic Voltammetry script*: In this case is important to start by selecting the cycle of the CV we are interested in. The second cycle is the one we will take into consideration, indeed the first one is for the electrochemical system to stabilize itself. Only those refined data corresponding to frames collected during the second cycle are considered. Let's now consider the cyclic voltammogram, the plot of the current (y-axis) versus the applied potential (x-axis) during each voltage sweep just for the selected cycle. The area under the current versus potential curve in this plot represents the charge that passes through the working electrode during the experiment.
  Then let's just consider the oxidation peak, for every sweep thanks to the function numpy.trapz the charge till 1.1 V and 1.2 V is calculated.

Then the scale values from the refined data are considered. A plot showing scale values in y axis and the corresponding voltage values in x axis is represented. Data have to be normalized so that all the potential sweeps can be compared. The normalization factor was calculated for every sweep considering an average of the scales data that corresponds to the potential interval 0.4-0.6V and 0.6-0.4V (double layer region). The exact same normalization is done on the data coming from the calculation of the area underneath the peak 200 of the diffraction patterns. The calculation of the area underneath the peak 200 is performed with the function numpy.trapz. A plot showing 200 peak area values in y axis and the corresponding voltage values in x axis is represented.

Then the scan rate and the 200 peak area value at 1.1 V and 1.2 V for every scan rate is registered.

3 | Results

The investigation of nanoparticles of Platinum used as catalyst in a PEMFC has garnered important answers regarding fundamental studies. X-ray diffraction stands as a powerful technique for elucidating the crystalline structure of nanoparticles. Following the protocol introduced in section 2.3, all the peaks in the Pt pattern have been fitted at the same time and the same structural model, Rietveld refinement. In this section, we present the outcomes of the data analysis, aiming to shed light on some features connected to structural properties of NP of Platinum.

3.0.1. Diffraction pattern

By subjecting a powder sample of Pt to XRD, a powder diffraction pattern is obtained, this pattern gives valuable information about the crystallographic structure of the powdered platinum sample. Indeed, thanks to powder diffraction it is possible to identify and characterize different crystalline solids, each of which produces a distinctive diffraction pattern [17]. A platinum powder diffraction pattern is characterized by a series of diffraction peaks, which represent the diffraction of X-rays by the crystalline planes within the sample. The positions of these peaks are usually expressed in terms of 2θ, which is the angle of diffraction. The diffraction peaks are often labeled using Miller indices (hkl), describing the orientation of crystallographic planes. Each of these peaks is characterize by a certain intensity that is related to the number of atoms in the crystallographic planes that give rise to that peak. Structural parameters extracted from the Rietveld analysis can be used to monitor Pt nanoparticles subjected to electrochemical processes, PS and CV. In particular for the scope of this study two structural parameters have been monitored, the lattice parameter and the peak area/scale.

3.0.2. Potential Step

The study of very small Pt NP's supported on carbon particles used as catalyst material in PEMFC has produced interesting results for what concerns the kinetics of fast fundamental processes taking place at the surface of those nanostructured electrocatalyst

electrodes. In particular, in this section, we will focus on the outcomes obtained monitoring the diffraction patterns resulting from the different potential steps enunciated in the table 2.1, specifically those ones detected with Pilatus 3X CdTe 2 M hybrid photon-counting area detector. Structural parameters extracted from the Rietveld analysis of those diffraction patterns have been plotted. In particular for every PS the lattice parameter and the scale have been taken into consideration. In each plot also the variation of the voltage applied has been taken into account. In the following, an example of the plots obtained from the refined data of the structural parameters corresponding to the PS identified as **S1-steps_12** in table 2.1.

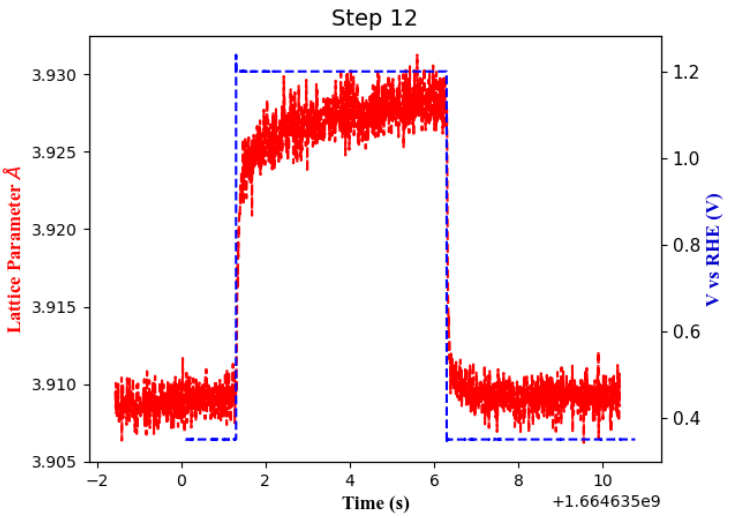

(a)

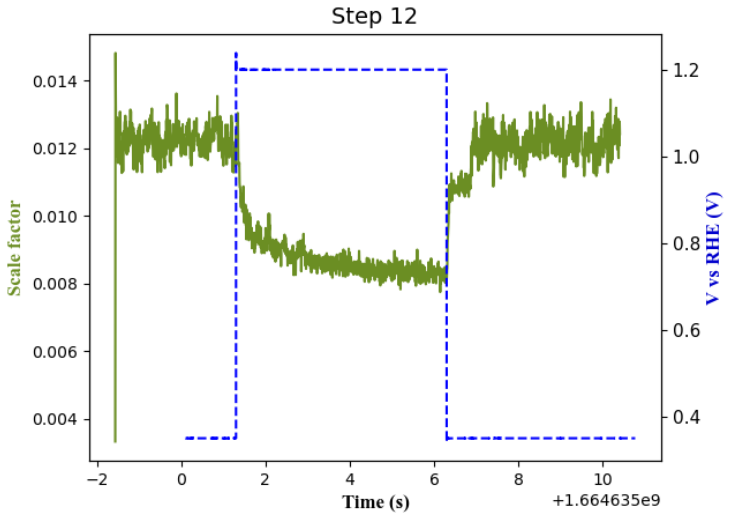

(b)

Figure 3.1: Structural parameters extracted from diffractograms collected holding the potential at 0.35V for 1.2s then going for 5s to 1.2V and then back to 0.35V for 10 s. Lattice parameter trend (red) following the steps of the potential (blue) (a), scale factor trend (green) following the steps of the potential (blue) (b)

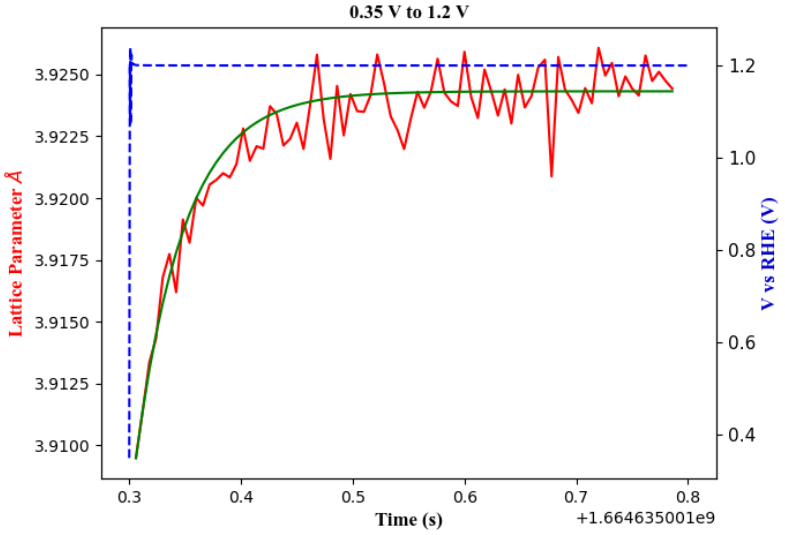

(a)

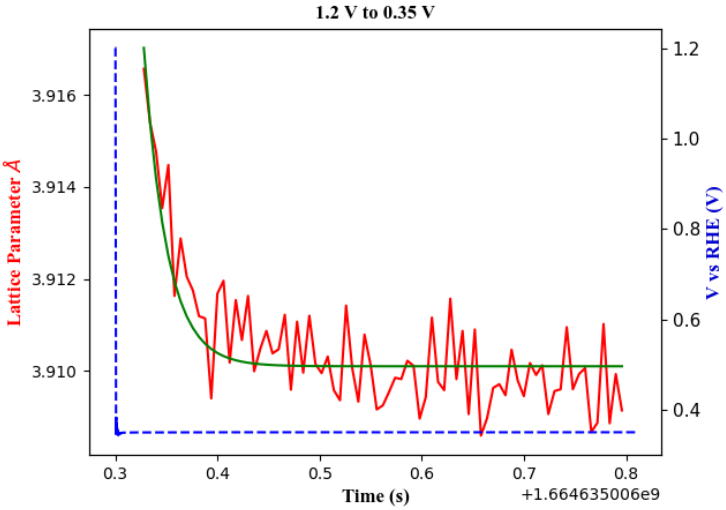

(b)

Figure 3.2: LP extracted from diffractograms collected stepping the potential from 0.35V to 1.2V (a) and from 1.2V to 0.35V (b). Lattice parameter(red) following the steps of the potential (blue) fitted with exponential(green).

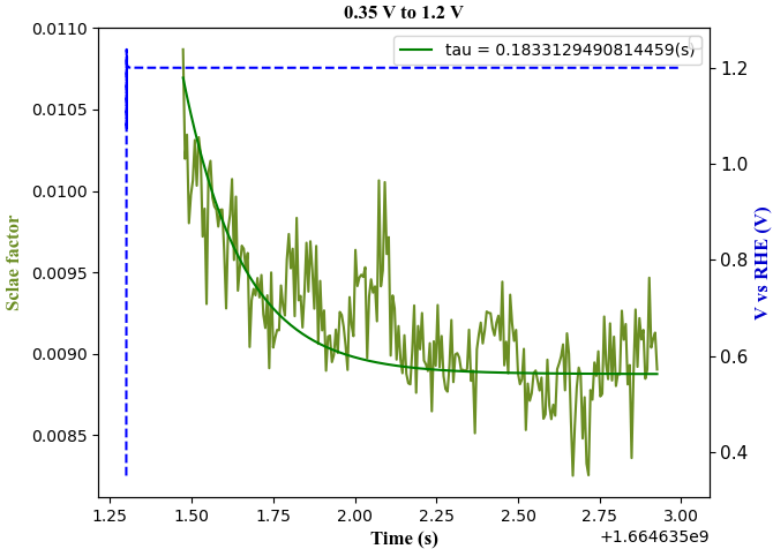

(a)

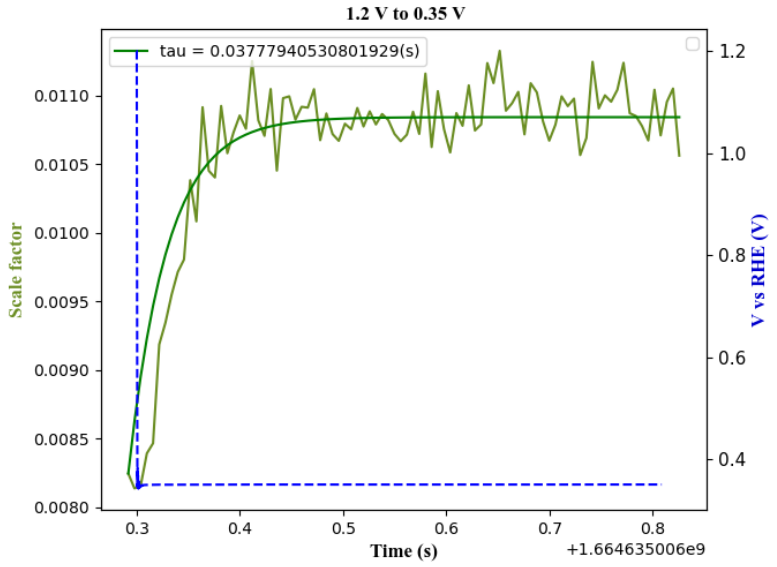

(b)

Figure 3.3: Scale factor extracted from diffractograms collected stepping the potential from 0.35V to 1.2V (a) and from 1.2V to 0.35V (b). Scale factor(dark green) following the steps of the potential (blue) fitted with exponential(green).

As already mentioned in section 2.3.4, a dedicated script for every PS performed has been written, with the aim of calculating the time constants that characterize the change of the lattice parameter both in charging and discharging phases, with charging phase we

mean the phase following the first step in potential and with discharging phase we mean the second step in potential (a more exhaustive explanation will be given in section 4). In the table 3.1 there is a sum up of the results obtained. Every set of PS done during the experiment has been analyzed, the lattice parameter has been monitored and in the following table the outcomes of the analysis are shown.

	Voltage (V)	Δ LP ($\AA$)	Tau up(s)	Tau down(s)
S1-steps_12	1.2	0.01483 ± 0.00014	0.04378 ± 0.00344	0.02264 ± 0.00350
S1-steps_15	0.9	0.00379 ± 0.00006	0.01090 ± 0.00353	0.00890 ± 0.00247
S1-steps_18	0.8	0.00384 ± 0.00006	0.00985 ± 0.00363	0.00712 ± 0.00402
S1-steps_20	0.7	0.00369 ± 0.00008	0.00998 ± 0.00328	0.00676 ± 0.00297
S1-steps_22	0.6	0.00157 ± 0.00010	0.00985 ± 0.00359	0.00699 ± 0.00348
S1-steps_24	0.5	0.00173 ± 0.00005	0.00841 ± 0.00500	0.00649 ± 0.00424
S1-steps_26	0.1	0.00444 ± 0.00007	0.02098 ± 0.00403	0.01996 ± 0.00390

Table 3.1: List of the results obtained from the analysis of the lattice parameter data corresponding to every potential step done during the experiment. In every PS the potential has been held at 0.35V for 1.2s, then stepped for 5s to the potential registered in the first column of the table and then back to 0.35V for 10 s. In the second column the variation in Angstrom of the lattice parameter corresponding to the variation of potential from 0.35 V to the value registered in the first column, see eq. 3.1. In the third and forth column there are the values in seconds of the time constants following, respectively, the increasing and the decreasing of the lattice parameter following the step up and the step down of the potential applied.

In figure 3.4 two plots show the results obtained though the data analysis performed on PS data. These two graphs show the consequences of the application of step potential to the FC. In particular, the plot 3.4a shows the values related to the time constants that characterize the change in value of the lattice parameter due to the application of a step potential. On blue the time constants related to the rising step, from 0,35 V to the value, in volts, indicated on the x axis and on orange the time constants related to the falling step, from the value, in volts, indicated on the x axis to 0,35 V. In the plot 3.4b we indicate with $\Delta Lattice\ Parameter$ the change in the lattice parameter of Pt nanoparticles, in particular

$$\Delta LatticeParameter = LP(x) - LP(0.35V) \tag{3.1}$$

where x is the value, in volts, indicated on the x axis of plot 3.4b.

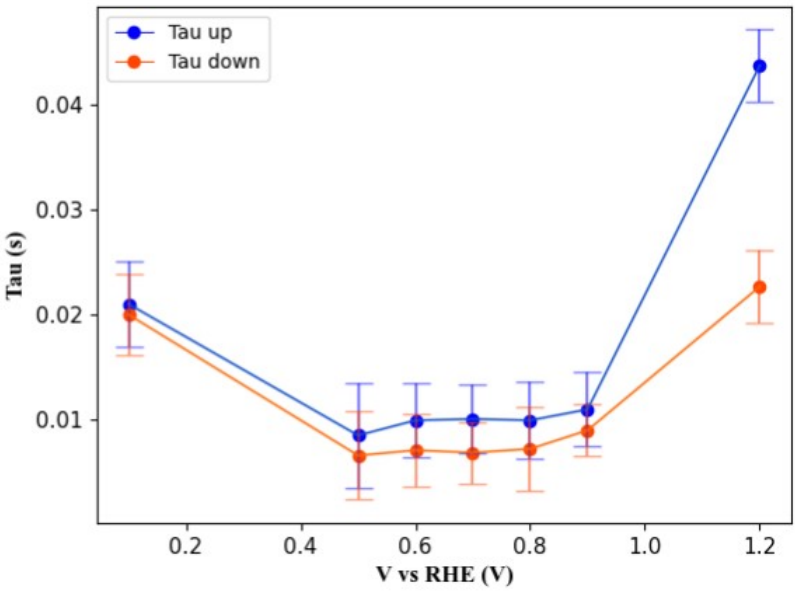

(a)

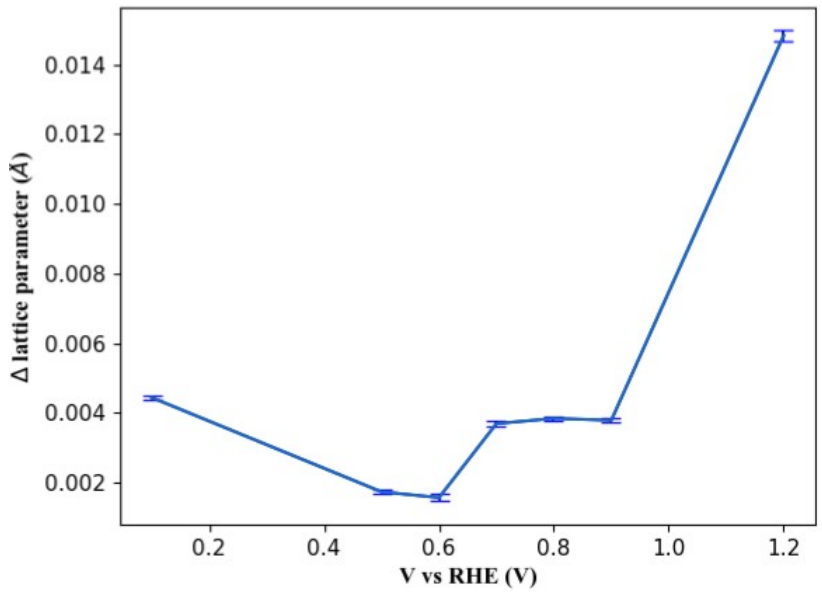

(b)

Figure 3.4: Graphs showing the results obtained from the PS analysis. The time constants calculated and registered in the third column (tau up) and fourth column (tau down) of table 3.1 are plotted, in x axis the value of the voltage at which the FC is stepped to. (a), the delta in Angstrom of the lattice parameter corresponding to the variation of potential from 0.35 V to the value of potential registered in x axis, this is the plot of the results registered in the second column of table 3.1(b)

3.0.3. Cyclic Voltammetry

The second part of our study consisted on studying the behaviour of the very small Pt NP's supported on carbon particles used as catalyst material in PEMFC when electrochemically we where applying CV. In particular, in this section, we will focus on the outcomes obtained monitoring the diffraction patterns resulting from the different CV enunciated in the table 2.2, specifically those ones detected with Pilatus 3X CdTe 2 M hybrid photoncounting area detector. In the following, figure 3.5, cyclic voltammograms are shown, the plot shows the (normalized) current (y-axis) versus the applied potential (x-axis) during each voltage sweep just for the selected cycle, the second one. Those data are collected from the BioLogic.MPRfile corresponding to each CV.

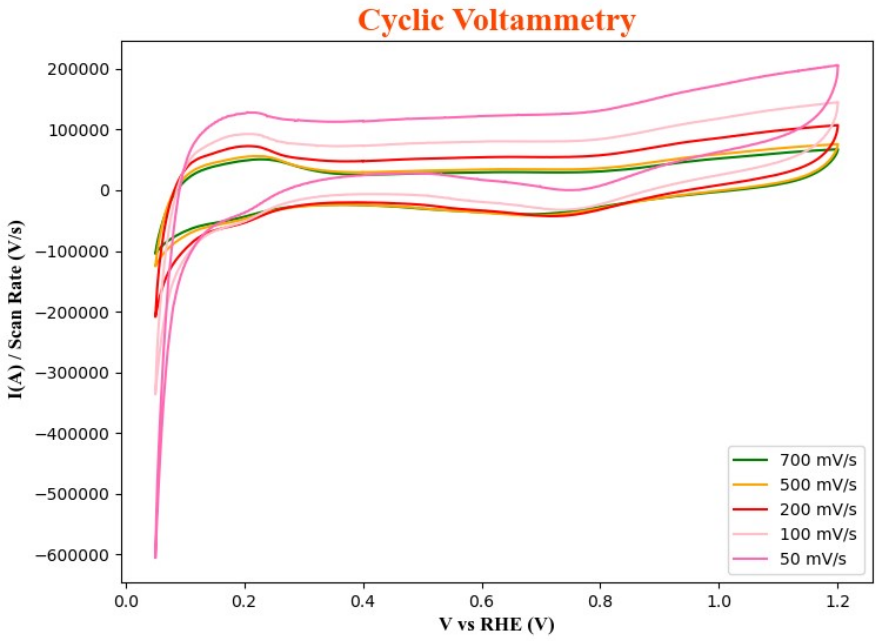

Figure 3.5: Cyclic voltammograms of Pt NP. Current densities have been normalized by dividing by the sweep rate.

Then the scale values from the refined data are considered. The following figure 3.6, shows the refined and normalized values of scale and 200 peak area coming from the CV performed at different voltage sweeps. To understand the normalization applied on these data go on the part named "Cyclic Voltammetry script" of section 2.3.4.

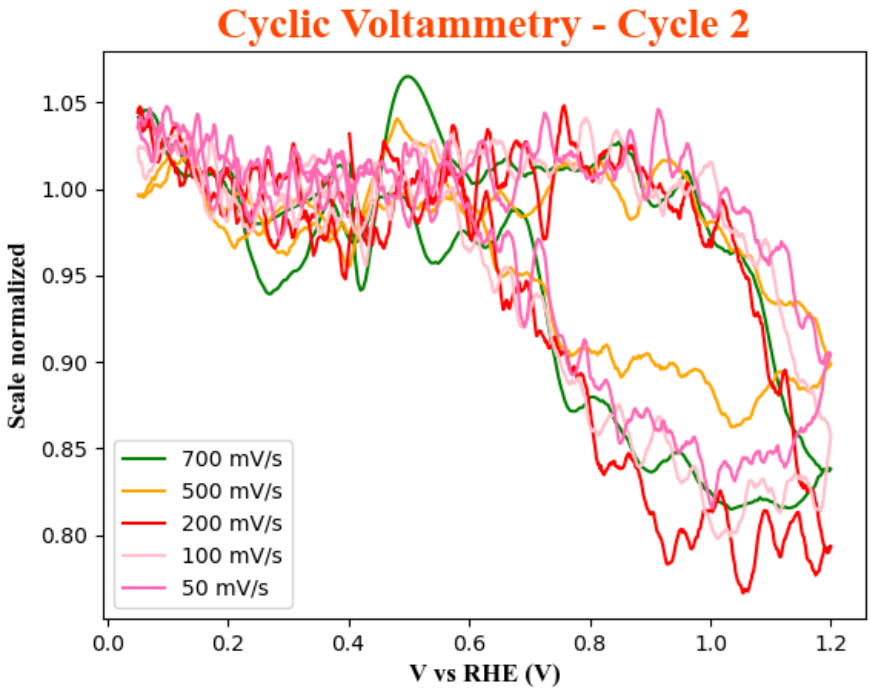

(a)

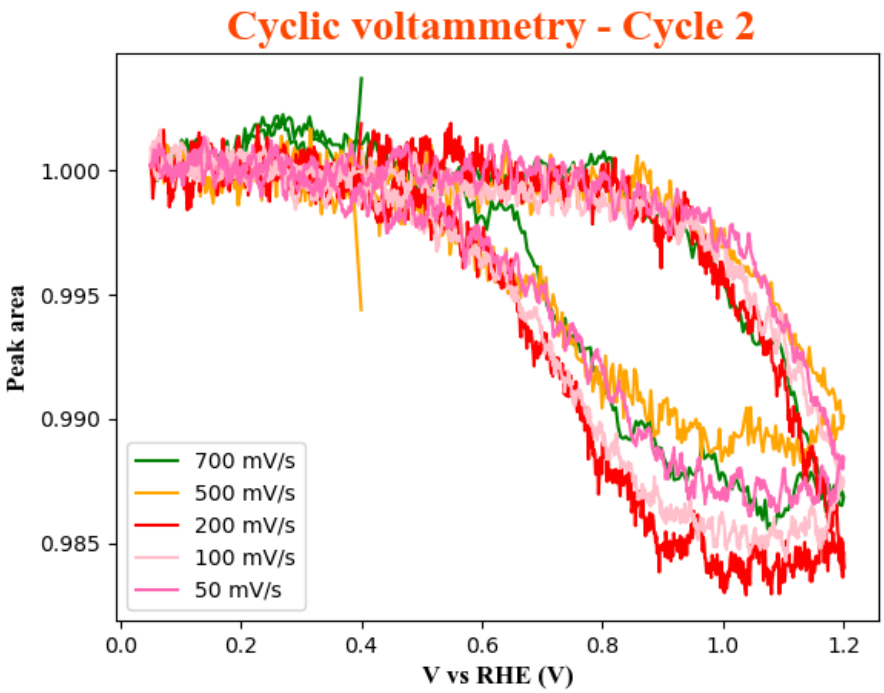

(b)

Figure 3.6: Graphs showing the results obtained from the CV analysis. The normalized scale values corresponding to different voltage sweeps are plotted in y axis, on x axis we find the corresponding voltage at which they have been registered. (a), The normalized 200 peak area values corresponding to different voltage sweeps are plotted in y axis, on x axis we find the corresponding voltage at which they have been registered.

Let's now focus our attention just on the oxidation peak, that peak that is visible in fig. 3.5 for every scan rate, it is the one extending from 0.9 V to 1.2 V. In the following, fig. 3.7, we find an overview of the charge, scale value and 200 peak area registered for every scan rate at the value of 1.1 V, which is in the oxidation peak.

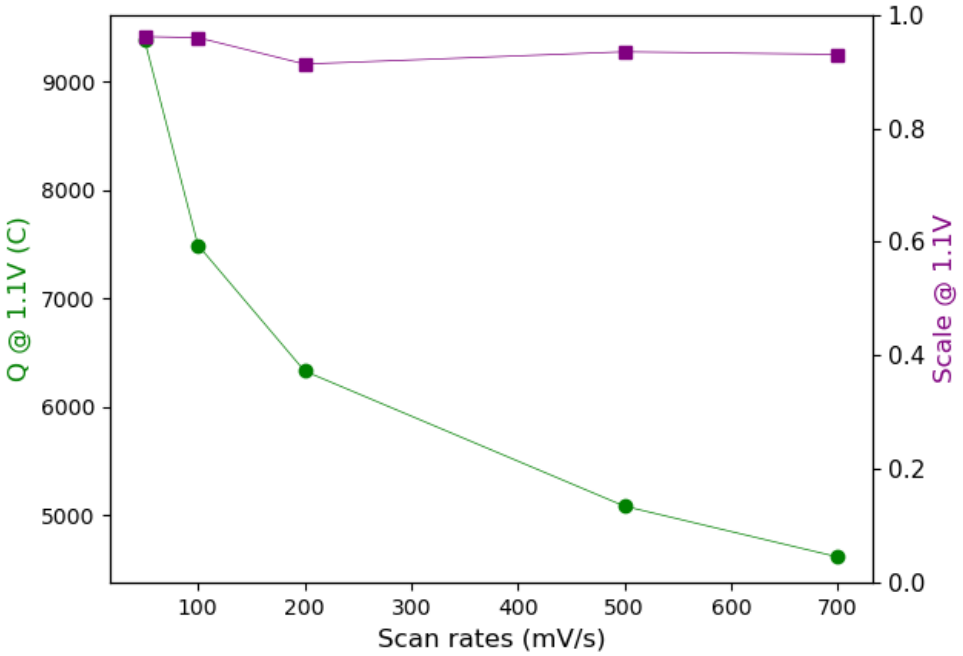

(a)

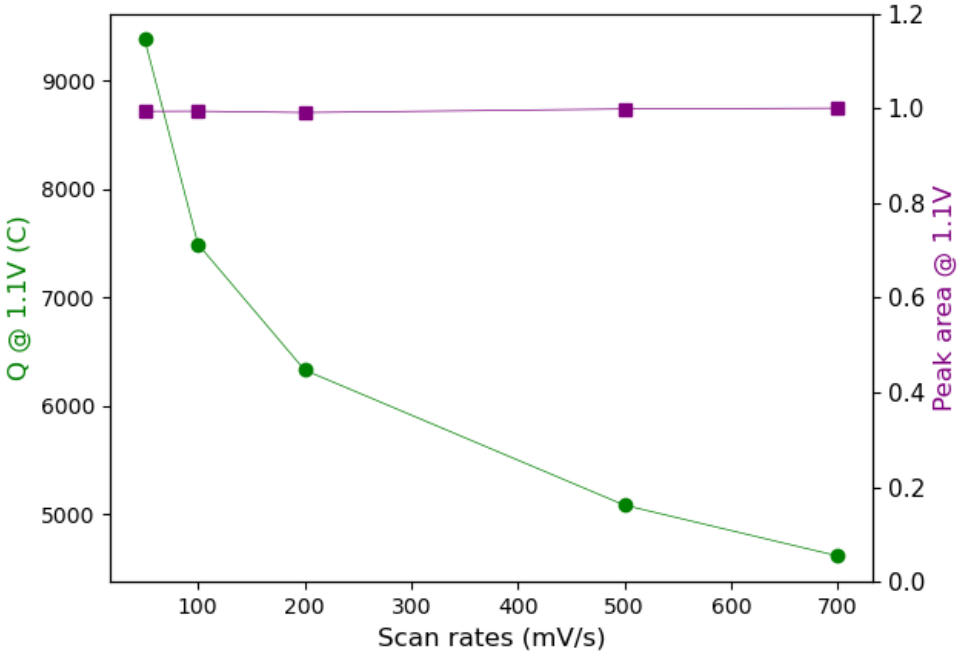

(b)

Figure 3.7: Charge collected in every CV considering the oxidation peak till a value of 1.1 V, in green. Then we distinguish in the plot (a) we have in purple the scale registered at 1.1V during cyclic voltammetry at various scan rates and in the plot (b) we have the 200 peak area registered at 1.1V during cyclic voltammetry at various scan rates and in the plot

4 | Discussion

The aim of this work is to better understand and characterize the kinetics of fast fundamental processes taking place at the surface of nanostructured electrocatalyst electrodes. In particular the study focused on double layer restructuring and adsorption/desorption of small molecules. The system used is a standard catalyst material used in low temperature hydrogen fuel cells, consisting of very small Pt NP's supported on carbon particles. In this section the results of this study will be interpreted and an explanation of their significance will be given.

4.0.1. Dynamics of Pt NP surface

We will now analyze those outcomes of the investigation previously introduced in section 3.0.2. With this scope let me start by showing the following plot, fig. 4.1, that is about the electrochemical behavior of Pt nanoparticles when subjected to a cyclic voltammetry experiment[19][41]. This cyclic voltammogram shows the usual features of platinum electrode, hydrogen evolution ($E < 0.05$ V vs RHE), underpotential absorption/desorption of hydrogen (HUPD, $0.05 \leq E \leq 0.30$ V vs RHE) and adsorption/ desorption of oxygenated species ($E \geq 0.50$ V vs RHE).
This plot is just a help to understand the reason why different potential steps have been performed.The red star present in this plot indicates the value in potential, 0.35V, from which every potential step done during the experiment were starting from. The pink dots reflect the values present in the first column of table 3.1, recalling that those are the different values in potential to which different PS were stepped to. The reason why these specific and different steps have been chosen is that they show distinct Pt surface chemistry.
The structural parameter chosen to track these changes in the sample microstructure is the lattice parameter. The lattice constant or the lattice parameter represents one of the fundamental physical dimensions that defines the geometric characteristics of unit cells within a crystal lattice. It is directly related to the distance between atoms in the crystal [41]. In the case of Pt that is a simple cubic crystal, this parameter corresponds to the size of the Pt unitcell, and it is therefore a direct measurement of the average Pt-Pt bond

length and crystallographic strain [34].
The fact that the lattice parameter breathes, meaning change in values following the step in potential is something we expected. Previous in situ electrochemical XRD studies[34] demonstrated that as the potential increases the LP starts to shift, testimony of two different processes happening on Pt surface. In particular the lattice parameter change can be explained by the strain induced by the adsorption of oxygenated species and the formation of the amorphous oxide layer that also makes a contribution to the total strain at the nanoparticle surface. However a quantitative understanding of the adlayer formation and place-exchange kinetics is normally limited by capacitive charging, meaning that oxidation or reduction at the electrode cannot occur until the voltage at the Pt surface has been established. The RC time constant of their electrochemical cell is approximately 1.5s. That's why the rate costants of fast adsorption and desorption of oxygenated species couldn't be calculated with a good accuracy. Only with a strategic compensation technique and fast data acquisition a more complete understanding of Pt nanoparticle oxidation and degradation phenomenon is possible. In our study compensation techniques have been adopted, see section 2.2.4, combined with the use of a fuel cell designed in order to guarantee fast diffusion of reactants to the electrode surface and very close electrodes, with the aim of overcoming the ohmic drop of the cell and obtain better results then before. And for a fast data acquisition we relied on Pilatus 3X CdTe 2 M hybrid photoncounting area detector.

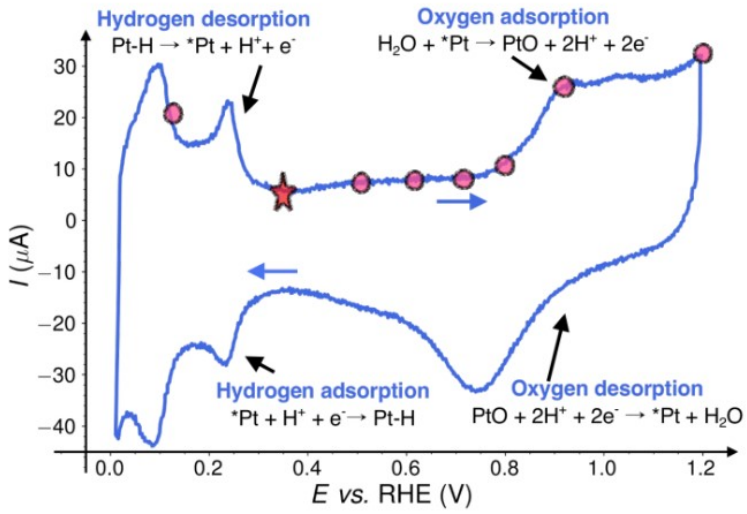

Figure 4.1: Cyclic voltamogram of Pt NP [19].The x-axis of represents the applied voltage, the y-axis represents the measured current. The red star indicates the 0.35 V potential that is the starting potential for every PS done. Each pink dot indicates the value in potential corresponding to each PS done.

Let's now compare the plot 3.4b and the Cyclic voltamogram of Pt NP, fig 4.1. In the first plot what is showed is the shift in modulus of the LP between the value assumed by LP once the potential is stepped to those values of potential indicated in pink dots in fig 4.1 and, the value of LP assumed when the potential of the electrode is set at 0.35V (red star). A trend is visible, the Δ of LP is higher for the right extreme of the plot 3.4b, for that value corresponding to a PS to 1.2 V. It shows minimum values for PS to 0.5V and 0.6V and comparable values for those PS to 0.1V, 0.7V, 0.8V and 0.9V.
The minimum values are reflecting PS in the double layer region. As we already seen in section1.2.1, when a electrode (Pt NP's supported on carbon particles) is in contact with an electrolyte, charges on the electrode surface attract ions from the electrolyte. When a voltage is applied to the electrode, the electrical double layer begins to charge. When the electrode potential becomes more positive, cations in the inner Helmholtz plane experience electrostatic repulsion. This results in the release of cations into the electrolyte. On contrary, anions from the electrolyte are attracted to the positively charged electrode surface, counterbalancing the charge. This migration of ions causes the electrical double layer to charge. The exact opposite happens when the electrode potential becomes more negative, cations are attracted back to the electrode surface, and anions are repelled. This leads to the discharge of the electrical double layer as it returns to a neutral state. In the double layer region, there are typically no oxidation or reduction of species occurring at

the electrode surface. Instead, the current is governed by the rate at which the double layer capacitance charges and discharges in response to changes in the applied potential. This is called capacitive current and it is testimony of what we call double layer reorganization, consequence of a change in electrochemical conditions. The time constant at which this process happens has been estimated.
By modeling the EDL as a capacitor it follows that the time constants characterising its charge and its discharge are exponential. A direct way to calculate them is by determining the time constants characterizing the change in lattice parameter. Specifically, the following equations are used, eq.4.1 and eq. 4.2.

$$y_c = \Delta LP * (1 - \exp - \frac{x_c - b_c}{\tau_{up}}) + LP(0.35V) \tag{4.1}$$

$$y_d = \Delta LP * \exp - \frac{x_d - b_d}{\tau_{down}} + LP(x) \tag{4.2}$$

Where eq. 4.1 describes the exponential growth of LP, y_c is the array of values of LP, ΔLP is the shift in LP, x_c is the array of values of time, τ_{up} is the charging time constant, LP(0.35 V) is the value of LP at 0,35 V. Eq. 4.2 describes the exponential decrease of LP, y_d is the array of values of LP, ΔLP is the shift in LP, x_d is the array of values of time, τ_{down} is the discharge time constant, LP(x) is the value of LP at the potential x, that is the potential at which the discharge starts. Those curves are perfectly fitting the shift in LP, indeed are those green exponential curves visible in the plots of fig. 3.2.
The minimum in shift of LP, minimum ΔLP, is typical of those PS in which the potential change just determines the reorganization of the DL, just capacitive current. In table 3.1 we find that the results for tau up, time constant of the charging of the DL, is 0.0084 $\pm$ 0.005 s. Whereas tau down, time constant of the discharging of the DL, is 0.0064 $\pm$ 0.0042 s.
In the plot 3.4b we notice a plateau for those PS from 0.35V to 0.7V, 0.8V, 0.9V. A greater Δ in LP, is due to the presence of another phenomenon: adsorption of oxygenated species. Another way of measuring the adsorption of oxygenated species could be the monitoring the scale parameter or the peak area, as this parameter is proportional to the total number of illuminated Pt unit cells in the metallic crystal lattice [34]. Nevertheless no step in the peak area has been noticed for those steps, confirming what already found in literature: the lattice parameter responds to the faster, initial step of adsorption of oxygenated species, while the peak area follow much slower phenomena. Higher values of time constants are observed in this case, for example the PS to 0.8V gives as tau up a value of 0.0098 $\pm$ 0.0036 s and as tau down a value of 0.0071 $\pm$ 0.004 s, confirming the fact that the Pt NP are ongoing other effect beside the DL reorganization.

Considering now the PS towards higher potential, 1.2V, we notice a greater value of ΔLP and greater tau up and tau down, respectively 0.0437 ± 0.0034 s and 0.0226 ± 0.0035 s. A shift in ΔLP is a testimony of a stretching of the average Pt-Pt bond length. By looking at 3.3b it is visible that in this case also the peak area (or scale) is sensitive to the step in the potential. Meaning that this is a sufficiently oxidizing step to initiate place exchange of the adsorbed oxygenated species and the growth of surface limited Pt oxide. The time constants of the change in the area are, tau up of 0.18 (s) and tau down of 0.038 (s). Each structural parameter exhibits a different rate constant, the time constants of the scale are telling about other mechanism involving the Pt NP.
Stepping the potential to lower values (<0.35 V), as 0.1V, a shift in the lattice parameter is observed. Also, it is observed that the time constants characterizing this PS are higher with respect to the case of the simple restructuring of DL, tau up is 0.0209 ± 0.0040 s and tau down 0.0199 ± 0.0039 s . This can be explained as a strain induced by the adsorption of underpotentially deposited hydrogen which is interestingly slower than OH (H-UPD).
In general we notice that all the time constants characterizing the falling step of the PS, tau down, are faster than those characterizing the rising step of the PS, tau up. Suggests the existence of a different kinetic state between charging and discharging processes. When we apply a falling potential step at the surface of Pt NP what happens is an oxygen desorption, this for those PS in which an oxygen asdorption was observed. In particular we notice a big difference between the two tau in the case of the PS to 1.2V.
Future work will focus on studying and analyzing those data collected with CCD Si based detector PCO DiMAX, this will help in getting better results since the diffraction patterns were collected at very high speeds (20kHz). All the time constants will be estimated again with higher precision.

4.0.2. Electrochemical oxidation

Following here, the results previously introduced in section 3.0.3 are interpreted and explained. Previous experiments conducted in ID31 [34] already produced important results regarding the dynamics of platinum surface oxide in FC. In that study cylic voltammetry experiments are conducted at various scan rates: 5mV/s, 10mV/s, 25mV/s and 50 mV/s. Indeed, the goal of the present study is to go beyond those scan rates, exploring higher potential sweeps.
In the plot showed in fig 3.5 a comparison between the second cycle of all the CV done during the experiment is showed. The second cycle is chosen because in previous studies [38], it has been shown that oxidation and reduction during the first cycle are important to get a clean surface that represents the actual catalytic properties of the catalyst. To

obtain relevant electrochemical information it is recommended to start by considering the second cycle. In this plot the intensity has been normalized by dividing it with the scan rate, this normalization is useful for comparing CV data obtained at different scan rates. By changing how fast the potential is swept, the current response changes. Sweeping the potential at highest speed translates in collecting less current. In particular during the forward sweep of the CV, when the voltage changes from 0.1V to 1.2V, oxidation reactions occur leading to the release of electrons from water molecules, the charge is considered positive and we see that the 50mV/s CV reached the highest values whereas the green line corresponding to the 700mV/s CV is at minimum. During the reverse sweep of the CV, as the voltage decreases from the upper potential limit to the lower potential limit, reduction reactions occur and faster sweep in potential reach highest peak in the hydrogen adsorption region.

Monitoring and analyzing the diffraction patterns during cyclic voltammetry experiments have produced the plots in figure 3.6. In particular noticing how noisy where the data in fig. 3.6a a further confirmation of the trend of the data is obtained by calculating the 200 peak area, fig. 3.6b. A calculation of the area of all the peaks would have take longer time so the 200 peak was chosen since normally it is a very sensitive peak to redox reactions and does not overlap with the background signal from the cell. To determine its area, a calculation of the area under the 200 peak of every diffraction pattern, normalized in intensity, was done.

Considering that slower sweep rates result in longer periods of time spent at high potentials, and considering the slow kinetics of PE, pointed out just before, normally systematically higher peak area (less oxidation) characterize faster sweep rates. This is not really visible in this graph. Hysteresis is observed in the region of the plots, fig. 3.6a and fig. 3.6b, between 0.7V and 1.2V, this because between oxidation path e reduction path we have a lot of differences. It is way more difficult to adsorb oxygen (forward scan) than to reduce it (reverse scan). This is not the case of hydrogen and double layer region which don't show hysteresis, we are referring to those values corresponding to a potential lower than 0.7V.

Before continuing with this discussion let's shed some light on the electrochemical oxidation of Pt [27]. For this scope we will focus on the anodic peak at 1,05V. In situ SXRD measurements on the oxidized Pt surface by You et al. showed that place exchange (PE) occurs in the region of this peak [43]. Further studies confirmed that the onset of X-ray intensity changes due to PE occurs precisely at the Pt oxide peak [27]. A correlation between PE with an electrochemical current it is assumed. The idea proposed in that study is that multiple Pt oxide species adsorbed, like OH and O, and subsurface oxygen, react in this potential region and that the relative coverages strongly depend on the total

surface coverages rather than the potential. Meaning that the Pt extraction, which is the first step of PE, depends on the local O coverage.
The Pt extraction was just studied at slow potential sweep rates and the decrease in X-ray intensity was seen to start approximately at potentials near the maximum of the anodic peak. This because, before the extraction is initiated there's the need of the production of certain number of local and stabilizing O atoms. However very recently high-energy surface X-ray diffraction (HESXRD) measurements on Pt(111) during fast cyclic voltammetry demostrated a new point of view to explain electrochemical oxidation [29]. By fast simultaneous electrochemical and in situ high-energy surface X-ray diffraction measurements it is demonstrated that the initial extraction of Pt atoms from Pt(111) is a fast, potential-driven process, whereas charge transfer for the related formation of adsorbed oxygen-containing species occurs on a much slower time scale and is evidently uncoupled from the extraction process.
With this is mind our study explores fast CV on Pt NP, which is an applied system, to check the validity of this hypothesis even for nanoparticulate material. In fig. 3.7 we see in both graphs the green line representing the charge collected in every CV at 1.1V, that is a potential value in the anodic peak. As the scan rates are faster the value of charge decreases, showing that the charge-transfer process is kinetically slow. In both graphs of fig. 3.7 we notice that both the scale value and the 200 peak area (purple lines), two values reflecting the the total number of illuminated Pt atoms in the metallic crystal lattice and so reflecting the presence of oxide on the surface, are constant through the different scan rates. This demonstrate that the fast extraction process depends very little on sweep rate, which shows that the extraction is driven by potential, independently of the adsorbed species around it. This give a confirmation of what already demonstrated in Pt(111) [29], electrochemical oxidation is therefore not coupled to the uptake of oxygen species and thus is inherently different from gas-phase thermal oxidation, which is driven solely by the oxygen's chemical potential.
Future work will focus on studying and analyzing those data collected with CCD Si based detector PCO DiMAX, this will help in getting better results since the diffraction patterns were collected at very high speeds (20kHz). The investigation will also continuing by investigating charge and scale factor at different point of the anodic peak.

5 | Conclusion

Platinum, stands as the most active element for numerous essential electrocatalytic reactions. Furthermore, in the context of electrochemical energy conversion and storage, such as in polymer electrolyte membrane fuel cells (PEMFCs), it maintains its status as the most important catalyst for applications and continues to serve as the standard for electrocatalyst materials. The development of studies aimed at understanding oxidation and reduction reactions happening on Pt-based nanocatalysts, are essential since those are key process affecting the stability and activity of Pt. Thereby directly impacting the efficiency of fuel cells.

High-energy X-ray diffraction serves as a convenient tool for examining these processes, as well as broader alterations in surface chemistry, offering high temporal resolution. Potential changes, like PS and CV, serve to study the kinetics of Pt nanoparticle surface chemistry and initial stage of metal electrooxidation. TOPAS software allowed the sequential refinement of Pt diffraction patterns collected in fast acquisition. Also, all the peaks in the Pt pattern are refined at the same time and with the same structural model, Rietveld refinement. Lattice parameter and scale factor are the two structural parameters in which we focused.

This approach allowed the detection of lattice strain, highlighted by the lattice parameter breathing corresponding to PS. This parameter has been seen sensitive to the adsorption of electro-active species on the surface. Instead, the scale factor parameter was seen to be sensitive only to the place-exchange step in the formation of Pt oxide. This in-depth study focused on the estimation of the time constants characterizing the electric double layer restructuring and adsorption/desorption of small molecules. This has been successfully done by fitting the shift of LP with exponential functions. In particular the time constant of the charging and discharging of the DL was determined, 0.0084 ± 0.005 s and 0.0064 ± 0.0042s respectively. Since the lattice parameter responds to the faster, initial step of adsorption of oxygenated species, time constants are estimated also in this case. For example the PS to 0.8V gives as tau up a value of 0.0098 ± 0.0036 s and as tau down a value of 0.0071 ± 0.004 s. Also, a strain induced by the adsorption of underpotentially deposited hydrogen is observed thanks to the PS to 0.1 V, the time constants

corresponding to this are tau up is 0.0209 ± 0.0040 s and tau down 0.0199 ± 0.0039 s. PS to 1.2V has been proven to be a sufficiently oxidizing step to initiate place exchange of the adsorbed oxygenated species and the growth of surface limited Pt oxide. Greater have been estimated in this case, tau up and tau down, respectively 0.0437 ± 0.0034 s and 0.0226 ± 0.0035 s.

The CV experiments conducted in this study on Pt NP, have been done to check the validity of a innovative hypothesis made in previous study, [29], on Pt (111), in this case the aim is to explore an applied system as this nanoparticulate material. The hypothesis is that the initial stage of metal electrooxidation is a complex process in which the electric potential itself plays a crucial role. The extraction of Pt atoms occurs rapidly, and the coverage of these extracted atoms is primarily determined by the potential, regardless of the coverage of adsorbed oxygenated species on the Pt surface. The confirmation of this arrives from the study of the scale factor parameter and 200 peak area. In particular the first parameter has been extracted from TOPAS with the same process done to extract structural parameters from PS diffraction patterns. The 200 peak area was calculated in Python directly from the Pt diffraction patterns, to confirm the validity of the results obtained with TOPAS. The both show a clear independence between extraction of Pt atoms and oxide coverage of the surface. Indeed, the scale factor/ 200 peak area remains constant for all the scan rates at 1.1V, whereas the charge clearly decreases as the scan rates become faster and faster. To accurately describe electrochemical oxidation processes, it is necessary to move beyond models focused solely on the solid-vacuum interface and explicitly acknowledge the role of the electrochemical double layer.

Bibliography

[1] www.esrf.fr. URL https://www.esrf.fr/BLISS.

[2] What is electrochemical impedance spectroscopy (eis)? URL https://www.biologic.net/topics/what-is-eis/.

[3] How does the esrf work? URL https://www.esrf.fr/home/education/what-is-the-esrf/how-doesthe-esrf-work.html.

[4] www.esrf.fr. URL https://www.esrf.fr/UsersAndScience/Experiments/StructMaterials/ID31.

[5] www.irena.org. URL https://www.irena.org/Energy-Transition/Outlook.

[6] www.dectris.com. URL https://www.dectris.com/detectors/x-ray-detectors/pilatus3/pilatus3-for-synchrotrons/pilatus3-x-cdte/.

[7] topas.webspace.durham.ac.uk. URL https://topas.webspace.durham.ac.uk/.

[8] www.biologic.net. URL https://www.biologic.net/potentiostat-galvanostat/?gclid=CjwKCAjwwb6lBhBJEiwAbuVUSiI-RN9mhGwS64NjQXiMCfFl5buGmD8ngdZPH_92i1nGCBPJpEaFuxoC87cQAvD_BwE&https%3A%2F%2Fwww.biologic.net%2Fwhy-potentiostats-galvanostats%2F.

[9] www.chemistryviews.org, . URL https://www.chemistryviews.org/details/education/1458465/How_Do_Fuel_Cells_Work/.

[10] www.energy.gov, . URL https://www.energy.gov/eere/fuelcells/hydrogen-and-fuel-cell-technologies-office.

[11] www.umicore.com, . URL https://www.umicore.com/en/newsroom/what-are-fuel-cells/.

[12] www.ceb.cam.ac.uk, . URL https://www.ceb.cam.ac.uk/research/groups/rg-eme/Edu/fuelcells/types-of-fuel-cells.

[13] Python fast azimuthal integration. URL https://pyfai.readthedocs.io/en/master/pyFAI.html.

[14] Lightsources.org. URL https://lightsources.org/.

[15] pd.chem.ucl.ac.uk. URL http://pd.chem.ucl.ac.uk/pdnn/diff2/kinemat2.htm.

[16] Innovaxn plenary event - michal ronovsky. URL https://www.youtube.com/watch?v=9SRhgYd2o4s.

[17] en.wikipedia.org. URL https://en.wikipedia.org/wiki/X-ray_crystallography.

[18] A.L.Brambilla. Lecture notes of physics of low-dimensional systems ii –experimental methods, 2021.

[19] C. Atlan, C. Chatelier, I. Martens, M. Dupraz, A. Viola, N. Li, L. Gao, S. Leake, T. Schülli, J. Eymery, F. Maillard, and M.-I. Richard. Imaging the strain evolution of a platinum nanoparticle under electrochemical control. *Nature Materials*, 22:754–761, 2023. doi: 10.1038/s41563-023-01528-x. URL https://hal.science/hal-04090004.

[20] T. Bednarek and G. Tsotridis. Assessment of the electrochemical characteristics of a polymer electrolyte membrane in a reference single fuel cell testing hardware. *Journal of Power Sources*, 473:228319, 2020. ISSN 0378-7753. doi: https://doi.org/10.1016/j.jpowsour.2020.228319. URL https://www.sciencedirect.com/science/article/pii/S0378775320306236.

[21] C. Benabderrahmane, J.-C. Biasci, J.-F. Bouteille, J. Chavanne, L. Farvacque, L. Goirand, G. Le Bec, S. Liuzzo, P. Raimondi, and F. Villar. Magnets for the ESRF-EBS Project. In *7th International Particle Accelerator Conference*, page TUPMB001, 2016. doi: 10.18429/JACoW-IPAC2016-TUPMB001.

[22] S. W. Boettcher, S. Z. Oener, M. C. Lonergan, Y. Surendranath, S. Ardo, C. Brozek, and P. A. Kempler. Potentially confusing: Potentials in electrochemistry. *ACS Energy Letters*, 6(1):261–266, 2021. doi: 10.1021/acsenergylett.0c02443. URL https://doi.org/10.1021/acsenergylett.0c02443.

[23] Y. Cai, W.-W. Wang, L. Wang, D. Liu, and F.-Y. Zhao. A proton exchange membrane fuel cell-compound thermoelectric system: Bidirectional modeling and energy conversion potentials. *Energy Conversion and Management*, 207:112517, 2020. ISSN 0196-8904. doi: https://doi.org/10.1016/j.enconman.2020.112517. URL https://www.sciencedirect.com/science/article/pii/S0196890420300534.

[24] R. Chattot, I. Martens, M. Mirolo, M. Ronovsky, F. Russello, H. Isern, G. Braesch, E. Hornberger, P. Strasser, E. Sibert, M. Chatenet, V. Honkimäki, and J. Drnec.

Electrochemical strain dynamics in noble metal nanocatalysts. *Journal of the American Chemical Society*, 143(41):17068–17078, 2021. doi: 10.1021/jacs.1c06780. URL https://doi.org/10.1021/jacs.1c06780. PMID: 34623136.

[25] B. Conway. Electrochemical oxide film formation at noble metals as a surface-chemical process. *Progress in Surface Science*, 49(4):331–452, 1995. ISSN 0079-6816. doi: https://doi.org/10.1016/0079-6816(95)00040-6. URL https://www.sciencedirect.com/science/article/pii/0079681695000406.

[26] A. H. B. Dourado. Electric double layer: The good, the bad, and the beauty. *Electrochem*, 3(4):789–808, 2022. ISSN 2673-3293. doi: 10.3390/electrochem3040052. URL https://www.mdpi.com/2673-3293/3/4/52.

[27] J. Drnec, D. A. Harrington, and O. M. Magnussen. Electrooxidation of pt(111) in acid solution. *Current Opinion in Electrochemistry*, 4(1):69–75, 2017. ISSN 2451-9103. doi: https://doi.org/10.1016/j.coelec.2017.09.021. URL https://www.sciencedirect.com/science/article/pii/S2451910317301187.

[28] J. S. O. Evans and I. R. Evans. Structure analysis from powder diffraction data: Rietveld refinement in excel. *Journal of Chemical Education*, 98(2):495–505, 2021. doi: 10.1021/acs.jchemed.0c01016. URL https://doi.org/10.1021/acs.jchemed.0c01016.

[29] T. Fuchs, V. Briega-Martos, J. O. Fehrs, C. Qiu, M. Mirolo, C. Yuan, S. Cherevko, J. Drnec, O. M. Magnussen, and D. A. Harrington. Driving force of the initial step in electrochemical pt(111) oxidation. *The Journal of Physical Chemistry Letters*, 14 (14):3589–3593, 2023. doi: 10.1021/acs.jpclett.3c00520. URL https://doi.org/10.1021/acs.jpclett.3c00520. PMID: 37018542.

[30] R. T. H.-G. H. Gerhard Hübschen, Iris Altpeter. *X-ray diffraction (XRD) techniques for materials characterization*. Woodhead, 2016. ISBN 9780081000403.

[31] A. Groß and S. Sakong. Modelling the electric double layer at electrode/electrolyte interfaces. *Current Opinion in Electrochemistry*, 14:1–6, 2019. ISSN 2451-9103. doi: https://doi.org/10.1016/j.coelec.2018.09.005. URL https://www.sciencedirect.com/science/article/pii/S2451910318301339. Bioelectrochemistry Electrocatalysis.

[32] L. Jacobse, V. Vonk, I. T. McCrum, C. Seitz, M. T. Koper, M. J. Rost, and A. Stierle. Electrochemical oxidation of pt(111) beyond the place-exchange model. *Electrochimica Acta*, 407:139881, 2022. ISSN 0013-4686. doi: https://doi.org/

10.1016/j.electacta.2022.139881. URL https://www.sciencedirect.com/science/article/pii/S0013468622000536.

[33] A. Lasia. Impedance spectroscopy applied to the study of electrocatalytic processes. In K. Wandelt, editor, *Encyclopedia of Interfacial Chemistry*, pages 241–263. Elsevier, Oxford, 2018. ISBN 978-0-12-809894-3. doi: https://doi.org/10.1016/B978-0-12-409547-2.13361-X. URL https://www.sciencedirect.com/science/article/pii/B978012409547213361X.

[34] I. Martens, R. Chattot, M. Rasola, M. V. Blanco, V. Honkimäki, D. Bizzotto, D. P. Wilkinson, and J. Drnec. Probing the dynamics of platinum surface oxides in fuel cell catalyst layers using in situ x-ray diffraction. *ACS Applied Energy Materials*, 2 (11):7772–7780, 2019. doi: 10.1021/acsaem.9b00982. URL https://doi.org/10.1021/acsaem.9b00982.

[35] I. Martens, A. Vamvakeros, R. Chattot, M. V. Blanco, M. Rasola, J. Pusa, S. D. Jacques, D. Bizzotto, D. P. Wilkinson, B. Ruffmann, S. Heidemann, V. Honkimäki, and J. Drnec. X-ray transparent proton-exchange membrane fuel cell design for in situ wide and small angle scattering tomography. *Journal of Power Sources*, 437:226906, 2019. ISSN 0378-7753. doi: https://doi.org/10.1016/j.jpowsour.2019.226906. URL https://www.sciencedirect.com/science/article/pii/S0378775319308997.

[36] N. D. M. Neil Ashcroft. *Solid State Physics*. Saunders College Publishing, 1976.

[37] R. Piazza. *Statistical Physics*. Springer Cham, Switzerland, 2016. ISBN 978-3-319-44536-6. doi: https://doi.org/10.1007/978-3-319-44537-3.

[38] M. Ronovsky, L. Pan, M. Klingenhof, I. Martens, L. Fusek, P. Kus, R. Chattot, M. Mirolo, F. Dionigi, H. Burdett, J. Sharman, P. Strasser, A. M. Bonastre, and J. Drnec. Assessing utilization boundaries for pt-based catalysts in an operating proton-exchange membrane fuel cell. *ACS Applied Energy Materials*, 6(17): 8660–8665, 2023. doi: 10.1021/acsaem.3c01243. URL https://doi.org/10.1021/acsaem.3c01243.

[39] M. M. V. Honkimäki. Upbl2, technical design report. Technical report, European Synchrotron Radiation Facility, 2013.

[40] K. Wille. *The physics of particle accelerators: An introduction*. 2000.

[41] E. S. Wolfgang Schmickler. *Interfacial Electrochemistry*. Springer Berlin, Heidelberg, Berlin, 2010. ISBN 978-3-642-04936-1. doi: https://doi.org/10.1007/978-3-642-04937-8.

[42] J. Wu. Understanding the electric double-layer structure, capacitance, and charging dynamics. *Chemical Reviews*, 122(12):10821–10859, 2022. doi: 10.1021/acs.chemrev.2c00097. URL https://doi.org/10.1021/acs.chemrev.2c00097. PMID: 35594506.

[43] H. You, D. J. Zurawski, Z. Nagy, and R. M. Yonco. In-situ x-ray reflectivity study of incipient oxidation of Pt(111) surface in electrolyte solutions. *The Journal of Chemical Physics*, 100(6):4699–4702, 03 1994. ISSN 0021-9606. doi: 10.1063/1.466254. URL https://doi.org/10.1063/1.466254.

List of Figures

List of Tables

List of Abbreviations

Acronym	Complete Name
ESRF	European Synchrotron Radiation Facility
BM	Bending Magnet
ID	Insertion Device
UHV	Ultra High Vacuum
RF	Radiation Frequency
SR	Synchrotron Radiation
PEEK	Polyether Ether Ketone
MEA	Membrane Electrode Assembly
CCM	Catalyst Coated Membrane
GDL	Gas Diffusion Layer
NP	Nanoparticles
PS	Potential Step
CV	Cyclic Voltammetry
PE	Place Exchange
LP	Lattice Parameter

Acknowledgements

I would like to express all my gratitude to my supervisor Dr. Jakub Drnec for the precious help during my internship at the ESRF in developing the project and for sharing with me all his knowledge, passion and experience in the field of Electrochemistry. I would like to thank all the team of the ID31 beamline of the ESRF for all the help, patience and kindness showed to me. This, added up to some beer sessions really made me feel welcomed. A special thank goes to Michal Ronovský, Hridya Nedumkulam, Andrea Sartori and Marta Mirolo for the special help with the experiment and data analysis. I would like to thank the ESRF, as a whole, that together with the Politecnico di Milano gave me the opportunity to work in the field for which I have studied and with people whose career is an example, as well as a stimulus, for me.

My sincere gratitude goes to the Politecnico di Milano, a very prestigious university that gave me the possibility of discovering a lot of this world and of my self. Teaching me the art of sacrifice and of dedication Politecnico gave to me glasses to see through the eyes of science.